

T CrB: overview of the accretion history, Roche-lobe filling, orbital solution, and radiative modeling

U. Munari¹, F. Walter², N. Masetti^{3,4}, P. Valisa⁵, S. Dallaporta⁵, A. Bergamini⁵, G. Cherini⁵, A. Frigo⁵, A. Maitan⁵, C. Marino⁵, G. Mazzacurati⁵, S. Moretti⁵, F. Tabacco⁵, S. Tomaselli⁵, A. Vagnozzi⁵, P. Ochner⁶, and I. Albanese⁶

¹ INAF National Institute of Astrophysics, Astronomical Observatory of Padova, 36012 Asiago (VI), Italy
e-mail: ulisse.munari@inaf.it

² Department of Physics and Astronomy, Stony Brook University, Stony Brook, NY 11794-3800, USA

³ INAF Osservatorio di Astrofisica e Scienza dello Spazio, via Gobetti 101, 40129 Bologna, Italy

⁴ Departamento de Ciencias Físicas, Universidad Andrés Bello, Fernández Concha 700, Las Condes, Santiago, Chile

⁵ ANS Collaboration, c/o Astronomical Observatory, 36012 Asiago (VI), Italy

⁶ Department of Physics and Astronomy, University of Padova, Asiago Astrophysical Observatory, 36012 Asiago (VI), Italy

Received June YY, 2025

ABSTRACT

Context. Expectations for an imminent new outburst of the recurrent symbiotic nova T CrB are mounting, initiated by the discovery in 2015 of a new enhanced mass-transfer phase (SAP), which is reminiscent of the one preceding the last recorded outburst in 1946.

Aims. We aim to derive a robust estimate of the most important parameters describing the physical nature of T CrB, trace the accretion history onto its white dwarf, and account for the unexpected delay in the occurrence of the new outburst: the SAP prior to 1946 was brighter, and it was followed by the nova eruption within 6 months from its conclusion. This time the 2015-2023 SAP has been fainter and two years past its conclusion no new eruption has yet taken place.

Methods. During 2005-2025, a period covering SAP and the preceding quiescence, we collected a massive amount of photometric and spectroscopic observations at optical wavelengths, that we have analyzed together with the abundant ultraviolet observations available in the archive of the *Swift* satellite.

Results. Guided by the results of the orbital solution and in particular by the radiative modeling to which we subjected the whole set of available data, we found for T CrB a binary period of 227.5528 days, an inclination of 61°, and masses of 1.35 M_⊙ and 0.93 M_⊙ for the white dwarf and the M3III companion, respectively, making mass transfer dynamically stable. The red giant fills completely its Roche lobe, and at $V_{\text{rot}} \sin i = 4.75 \pm 0.26 \text{ km s}^{-1}$ it is rotating much slower than the 16 km s⁻¹ co-rotation value. The ~20° azimuth of the hot spot, implied by the hump shaping the optical light curve in quiescence, fixes the outer radius of the disk to ~58 R_⊙, the same as the canonical value expected from disk theory. In quiescence the disk is cold and mostly neutral. SAP has been caused by an inside-out collapse of the disk, during which the mean accretion rate onto the WD has been ~28× larger than in quiescence. SAP ended in late April 2023, but from May 2024 mass-flow has intensively resumed at disk inner radii while the collapse wave reached the outer portions of the disk; the consequent revamp in mass accretion could fill the gap inherited by the fainter 2015-2023 SAP and eventually lead the WD accreted shell to ignition.

Key words. binaries: symbiotic – novae, cataclysmic variables – Stars: individual: T CrB – Accretion, accretion disks

1. Introduction

T CrB is a famous symbiotic nova, i.e. an otherwise normal nova (powered by explosive thermonuclear burning) that erupts within a symbiotic binary (see Munari 2025, for a recent review on symbiotic novae). It had outbursts observed in 1866 and 1946 (see the detailed summary by Kenyon 1986, and references therein), and possibly others recorded in ancient times (Schaefer 2023b).

After the return to quiescence following the 1946 outburst, T CrB has lived a quiet life spent accreting on the white dwarf (WD) at (very) low rates, with just some weak emission in H α generally visible on the optical spectra otherwise dominated by the absorption spectrum of the M3III red giant (RG) companion. On rare occasions (Iijima 1990; Anupama & Prabhu 1991; Hric et al. 1998), a temporary surge in accretion powered stronger emission in the lines and the Balmer continuum. As described by Munari et al. (2016), in 2015 T CrB drastically changed its status, when it entered a phase of enhanced mass-transfer which was reminiscent of a similar event,

lasting about eight years, which preceded the 1946 outburst (Payne-Gaposchkin & Wright 1946). For reasons of continuity with earlier studies of T CrB, we will keep calling "SAP" this phase of enhanced mass-transfer onto the WD which precedes an outburst, even if its original meaning of 'super-active accretion phase' has in the meantime evolved. The appearance of SAP lead Munari et al. (2016) to consider a new outburst of T CrB as probable for 2025-2026, a view which has been since shared by many others (e.g. Luna et al. 2020; Zamanov et al. 2023; Schaefer 2023a; Maslennikova et al. 2023). This has had the beneficial results of spurring intense pre-eruption monitoring of T CrB and the submission of ready-to-be-triggered proposals to most of the ground and space observing facilities. Such an alertness from the community, the expected $V \sim 1.5/2.0$ mag peak brightness (Kukarkin 1946; Shears 2024), and the proximity of T CrB to us (0.92 kpc according to Gaia DR3 parallax; Gaia Collaboration 2016, 2023), with all probability will results in such a wealth of multi-wavelength information to keep people busy for long in understanding and modeling them, leading to a

Table 1: Our *UBVRI* photometry of T CrB. The second columns provides the HJD–2400000. The full table is available only electronically via CDS, a small portion is shown here for guidance on its form and content.

Date	HJD	<i>V</i>	err	<i>U</i> – <i>B</i>	err	<i>B</i> – <i>V</i>	err	<i>V</i> – <i>R</i>	err	<i>V</i> – <i>I</i>	err	ID
2024-01-10.192	60319.692	9.897	0.008	0.431	0.006	1.446	0.014					1402
2024-01-11.114	60320.614	9.944	0.010	0.412	0.024	1.389	0.009					1402
2024-01-11.139	60320.639	9.935	0.005			1.425	0.007	1.124	0.008	2.543	0.022	0310
2024-01-12.141	60321.641	9.950	0.010	0.440	0.018	1.401	0.007					1402
2024-01-13.110	60322.610	9.966	0.011	0.763	0.018	1.443	0.009					1402
2024-01-13.164	60322.664	9.943	0.006			1.415	0.022	1.149	0.009	2.528	0.016	0310
2024-01-14.107	60323.607	9.948	0.010	0.503	0.015	1.456	0.016					1402
2024-01-14.163	60323.663	9.922	0.007			1.456	0.006	1.116	0.006	2.606	0.018	0310
2024-01-15.170	60324.670	9.967	0.008	0.410	0.007	1.366	0.009					1402
2024-01-16.121	60325.621	9.986	0.010	0.603	0.011	1.411	0.016					1402

significant leap forward in our understanding of novae in general and their symbiotic subclass in particular.

The SAP phase of T CrB ended in 2023 (Munari 2023b), lasting for about the same eight years as the one that preceded the 1946 eruption. In this paper we review, on the basis of a massive and multi-wavelength observational effort we carried out on T CrB, the (i) global properties of the 2015–2023 SAP in comparison with the long-term preceding quiescence, (ii) the amount of mass-flow through the disk to be subsequently accreted by the WD, (iii) the reformation of a steady disk following its collapse during SAP, (iv) revisit of the orbital solution, mass function, and constraints on the orbital inclination, and finally (v) structure, extent and evolution of the disk during quiescence and SAP as derived by radiative modeling.

2. Observations

The closing date for inclusion of new observations into the present paper is May 3rd, 2025.

2.1. *UBVRI* photometry

BVRI photometry of T CrB has been regularly obtained since 2005 with various ANS Collaboration telescopes, while the Asiago Schmidt 67/92cm telescope (which has an optical train completely transparent to near ultraviolet wavelengths down to the atmospheric cut-off) has been used primarily for *U*-band observations. All telescopes observed T CrB in all bands at each visit. All the photometry has been transformed from the local instantaneous photometric system to the Landolt (1992, 2009) standard system via color equations solved for all frames of each night via the *UBVRI* reference sequence located around T CrB and calibrated by Henden & Munari (2006). The same reference photometric sequence and the same observing/reduction procedures (Munari et al. 2012; Munari & Moretti 2012) have been similarly adopted at all telescopes over all nights, ensuing a high degree of homogeneity over the entire 2005–2025 photometric dataset. The collected photometric data are listed in Table 1, where the quoted uncertainties are the total error budget (TEB), which quadratically combine the Poisson error and the error associated with the transformation to the standard system via the color equations (usually the dominating term). Median values for TEB are 0.009 for *V*, 0.012 for (*B* – *V*), 0.013 for (*V* – *R*), 0.012 for (*V* – *I*), and 0.012 for (*U* – *B*). The total number of *UBVRI* runs is 712, which are distributed over 581 different nights. The corresponding lightcurves are plotted in Fig. 1, where the large scatter of plotted data is not due to errors but is instead a man-

ifestation of the orbital modulation and the large flickering persistently affecting T CrB.

The number of points in the *U*-band lightcurve of Fig. 1 has been increased by adding the results of integrating the *U* magnitude on the low resolution Asiago 1.22m + B&C spectra (see sect. 2.2 below), which are characterized by high S/N, blue wavelength limit around 3200 Å, and excellent fluxing. The band transmission profiles of Landolt (1992) have been adopted, with the flux zero-points taken from Bessell et al. (1998). Before computing the *U* magnitude, the flux zero-point of the spectra have been scaled so that the computed *B* magnitude equals that of conventional photometry from Tab. 1. To estimate the uncertainty of such a procedure in deriving the *U* band magnitude, we have observed over different nights and with the same instrumentation and data handling procedures about a dozen standard stars of a red color similar to T CrB (*B* – *V* ≥ 0.7), selected from Landolt (2009). The *U* magnitude so computed from the spectrum did match the tabulated one within 0.1 mag, which is fully adequate for the aims of the present paper.

2.2. Spectroscopy

A similarly large effort has been conducted in recording spectra of T CrB over 2011–2025 with telescopes located in Asiago, CTIO and Varese. The spectroscopic data presented in this paper will be made public available via CDS.

Low resolution spectroscopy of T CrB has been obtained over 2011–2025 with the Asiago 1.22m + B&C telescope, which has an optical train completely transparent to near ultraviolet wavelengths down to the atmospheric cut-off. The detector has been an Andor iDus DU440 CCD camera (2048×512 pixels, 13.5×13.5 μm each), which is characterized by a high near-UV sensitivity. A 300 ln/mm grating blazed to 5000 Å allowed to cover the 3200–8000 Å range at 2.31 Å/pix dispersion. The slit was set to a width of 2 arcsec and has always been rotated to the parallactic angle for optimal flux calibration against the spectrophotometric standards observed each night. The slit height of ~8 arcmin allowed a careful sampling and subtraction of the sky background.

High resolution spectra of T CrB were recorded with the Asiago 1.82m telescope + REOSC Echelle spectrograph. The 3550–7100 Å interval is covered in 32 orders without inter-order gaps by an Andor DW436-BV camera (housing an E2V CCD42-40 AIMO CCD, with 2048×2048 array, and 13.5 μm pixel size). The resolving power is 20,000 for the standard 2-arcsec slit-width. The slit height of 22 arcsec allows recording free 8 arcsec on

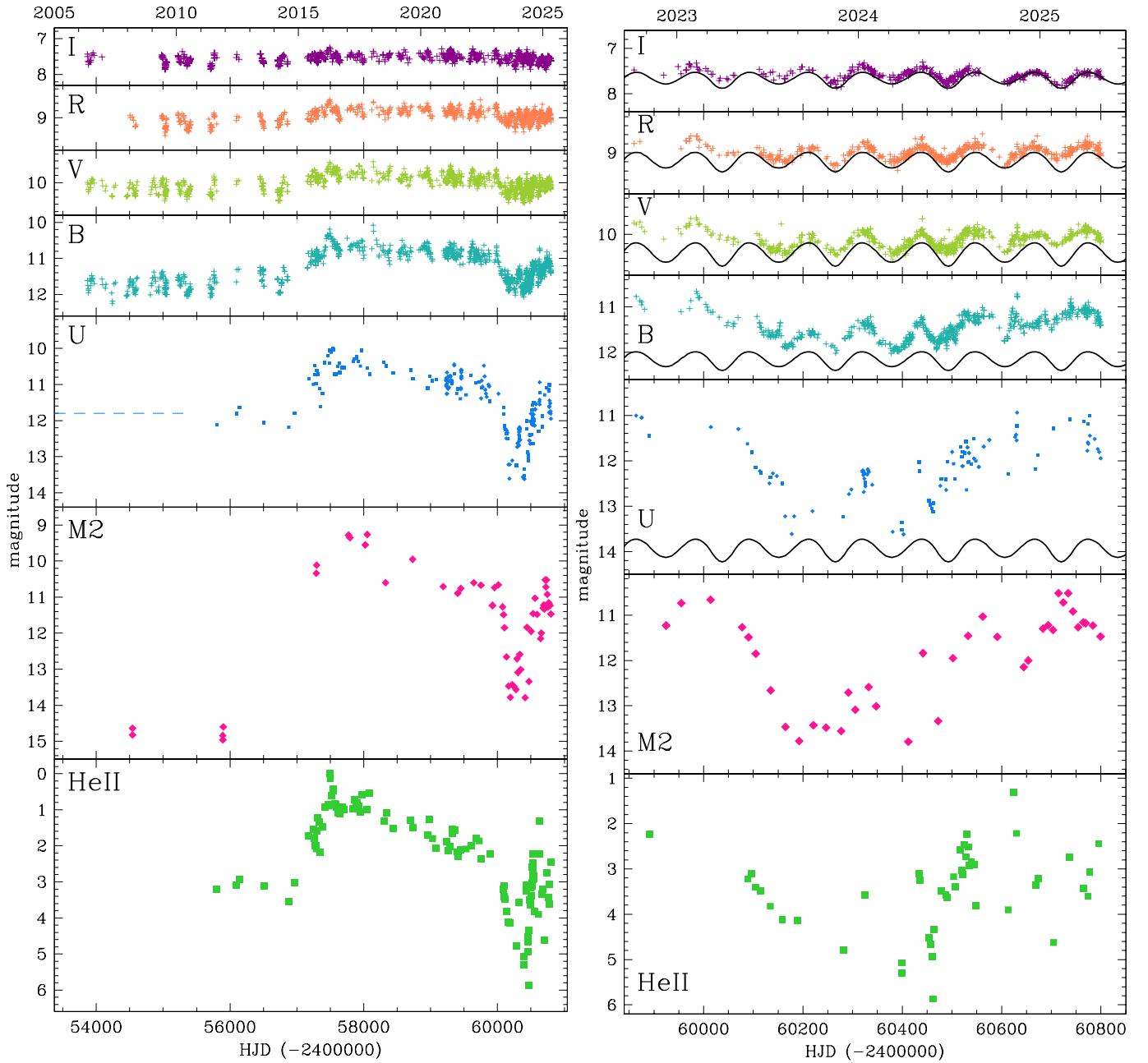


Fig. 1: Photometric evolution of T CrB over the last 20 years, with the panels at right zooming on the last four orbital revolutions. *UBVRI* data are from the ANS Collaboration monitoring program, M2 is the UVOT band from the *Swift* satellite, and the flux of the HeII 4686 emission line is expressed in magnitudes relative to the peak value ($F_{\text{max}} = 4.42 \times 10^{-12} \text{ erg cm}^{-2} \text{ s}^{-1}$; see sect. 4 for details). The sinusoidal curves at right is the lightcurve in that band of the bare, ellipsoidal distorted red giant without contribution from the stream, the hot spot, and the accretion disk (see the radiative modeling in sect. 7 for details).

both sides of the stellar spectrum for a careful definition of the sky background to subtract.

Echelle spectra of T CrB were also obtained with the Varese 0.84 m telescope, equipped with a long-slit mark.III Multi-Mode Spectrograph from Astrolight Instruments. The camera is a SBIG ST10XME CCD and the 4250–8850 Å range is covered in 32 orders without inter-order gaps. A 1×1 binning and the 2.0 arcsec slit width provide a resolving power $\sim 17,000$.

We also observed T CrB from CTIO in Chile, where it transits low over the northern horizon, using the CHIRON (Tokovinin et al. 2013) fiber-fed bench-mounted Echelle spectrograph mounted on the 1.5 m telescope operated by SMARTS.

We used CHIRON in "fiber" mode with 4×4 on-chip binning yielding a resolution $\lambda/\Delta\lambda \sim 27,800$. Typical Chiron exposure times were 10 minutes.

All spectra acquired with the Asiago and Varese telescopes have been reduced in IRAF, with all standard steps involving correction for bias, dark and flat frames, sky subtraction, wavelength and flux calibration. Chiron spectra have been similarly reduced using software written in IDL¹. As Chiron is fed by a single 2.5 arcsec diameter fiber, simultaneous sky subtraction is not possible. Under clear sky conditions, for a target as bright

¹ https://www.astro.sunysb.edu/fwalter/SMARTS/CHIRON/ch_reduce.pdf

as T CrB, this is an issue only in the vicinity of bright night sky lines, such as the Na D lines and [O I] 6300. Flux calibration is performed order-by-order using spectra of μ Col to establish the instrumental response, and orders are stitched together. There are five inter-order gaps longward of 8260 Å. Correction to absolute fluxes depends on sky conditions, and is accomplished by comparison with contemporaneous optical photometry.

2.3. Swift satellite ultraviolet observations

In order to complement our optical ground-based observations with ultraviolet (UV) data, we selected a series of pointing performed over nearly two decades, between 2008 and 2025, with the UltraViolet Optical Telescope (UVOT; Roming et al. 2005) onboard the *Neil Gehrels Swift* satellite (Gehrels et al. 2004). These observations were downloaded from the ASI-SSDC archive² and were chosen to be as close to simultaneous as possible to specific optical spectrophotometric epochs we collected during this time range. UV observations were acquired in the *UVW1*, *UVM2* and *UVW2* filters, with reference wavelengths 2600, 2246 and 1928 Å respectively (see Poole et al. 2008; Breeveld et al. 2011, for details).

All data were reduced within the *FTOOLS* environment (Blackburn 1995). Count rates on Level 2 (i.e., calibrated and containing astrometric information) UVOT images of T CrB were measured through aperture photometry within a 5'' radius centered on the source position, whereas the corresponding background was evaluated for each image using several circular regions in source-free nearby areas. The UV magnitudes were then determined using the *UVOTSOURCE* task and were calibrated using the UVOT photometric system described by Poole et al. (2008); the most recent fixings (2020 November) recommended by the UVOT team were taken into account and a check to reject small scale sensitivities³ was also performed. Furthermore, to the UV images in which the object was saturated we applied the criterion of Page et al. (2013) to determine the corresponding magnitudes from the readout streaks produced by the source.

A summary of the UV observations used in this paper, together with the corresponding results, is presented in Table A.1.

3. Reddening

The high +48° Galactic latitude implies a low reddening affecting T CrB, as supported by published values like $E_{B-V}=0.15$ by Cassatella et al. (1982) and $E_{B-V}=0.07$ by Nikolov (2022), or the $E_{B-V}=0.056$ upper limit by Schlafly & Finkbeiner (2011).

Here we apply an independent method to derive the interstellar reddening. All our Chiron Echelle spectra of T CrB were recorded in fiber mode at a resolving power of $\sim 27,800$, except one. The spectrum for 2022-08-16 was recorded in slicer mode, boosting the resolving power to $\sim 78,000$. Such a high value and the large barycentric velocity of T CrB allows to disentangle the NaI line profile into the stellar and interstellar components, as illustrated in Fig. 2 where the profile is fitted with a combination of three narrow Gaussians (the other NaI line at 5896 Å shows an identical profile).

The bluest of the three fitting Gaussian traces the stellar component at a measured heliocentric velocity of -28.5 km s⁻¹ well matching the velocity of the red giant from the orbital solution derived below in sect. 6. The other two components are

of interstellar origin, and are characterized by heliocentric velocities of -22.0 and -15.0 km s⁻¹, with equivalent widths of 0.1848 and 0.0551 Å, respectively. Adopting the calibration of Munari & Zwitter (1997), these equivalent widths translates into 0.060 and 0.015 reddening values, for a total $E_{B-V}=0.075$ interstellar extinction affecting T CrB, that we will adopt in this paper and which sits in the middle of the range of reddenings reported in literature. At such a low reddening, no other interstellar feature (atomic KI or diffuse interstellar bands) is strong enough for a fruitful measurement or even detection.

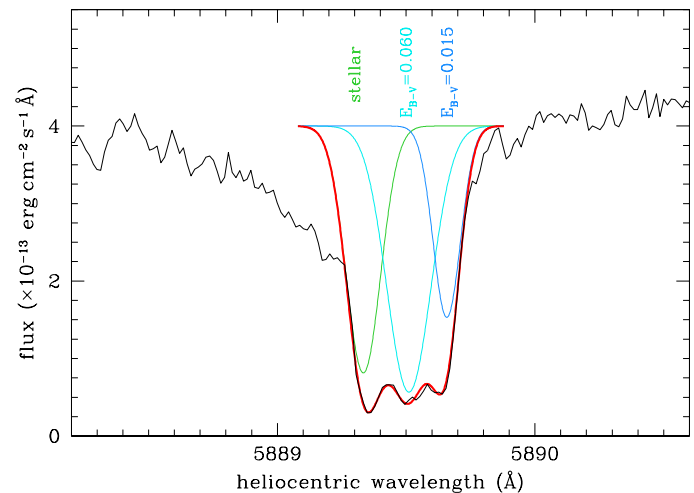


Fig. 2: Part of the Chiron spectrum of T CrB for 2022-08-16, recorded in slicer mode for a resolving power of $\sim 78,000$. The NaI line at 5890 Å is deconvolved into the stellar component (at -28.5 km s⁻¹ heliocentric velocity) and additional two of interstellar origin (at -22.0 and -15.0 km s⁻¹), with indication of the corresponding interstellar reddening.

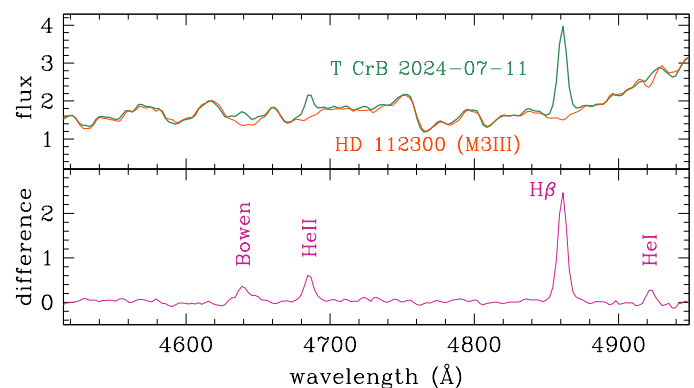


Fig. 3: To detect the presence of weak emission lines in the spectra of T CrB, it is necessary to subtract a scaled spectrum of an M3III template. *Top panel*: portion of Asiago 1.22m + B&C + 300 ln/mm spectra of T CrB and the M3III template HD 112300. *Lower panel*: the subtracted spectrum reveals the presence of emission lines other than H β . The ordinates are in 10^{-13} erg cm⁻² s⁻¹ Å⁻¹ on both panels.

4. The long-term evolution of T CrB

The photometric evolution of T CrB over the last twenty years is plotted in Fig. 1. The dashed horizontal line in the *U*-band

² <https://www.ssdsc.asi.it>

³ https://swift.gsfc.nasa.gov/analysis/uvot_digest/sss_check.html

panel marks the median quiescence brightness of T CrB as derived from published observations (e.g. Raikova & Antov 1986; Munari et al. 1992; Zamanov & Zamanova 1997; Hric et al. 1998; Zamanov et al. 2004; Henden & Munari 2008). The panels at right of Fig. 1 offer an expanded view onto the last ~ 4 orbits of T CrB, covering the post-SAP phase. The continuous curves in each panel show the lightcurve as expected from the sole ellipsoidal distorted red giant. These curves have been computed as part of the radiative modeling performed below in sect. 7, to provide a term of comparison against which to evaluate the contribution of all other components combined (WD, accretion disk, ionized RG wind, etc.).

To highlight the strict parallelism between accretion-driven photometric brightness and the spectral appearance, the bottom panel of Fig. 1 presents the flux evolution of the HeII 4686 emission line as measured on our Asiago 1.22m + B&C + 300 ln/mm grating spectra. For a direct comparison with the photometric magnitudes, in Fig. 1 the flux of the HeII 4686 emission line is also expressed in magnitudes ($-2.5 \times \log[\text{Flux}/F_{\text{max}}]$), relative to the peak value $F_{\text{max}} = 4.42 \times 10^{-12} \text{ erg cm}^{-2} \text{ s}^{-1}$, which has been reached on our spectrum for April 3, 2016. The flux of HeII 4686 emission line has been measured on our Asiago spectra *after* the subtraction of a template M3III spectrum (HD 112300) obtained with the same instrumentation and set-up, as illustrated in Fig. 3, a procedure necessary to provide cleaner and unbiased results, and which allows detection of HeII at its faintest levels.

Four phases are clearly distinct in the photometric and spectroscopic evolution of T CrB shown in Fig. 1, with corresponding representative spectra presented in Fig. 4:

- (1) the tail, extending to May 2014, of the long quiescence following the last outburst in 1946, with the spectrum for 2012-09-03 being representative of typical appearance during this protracted quiescence,
- (2) the enhanced mass-transfer phase (SAP), starting in the second half of 2014, peaking in brightness in May 2016 (cf. the spectrum for 2016-05-26) and smoothly declining (cf. the 2021-05-25 spectrum) through early 2023,
- (3) a post-SAP deep minimum, with *U*-band brightness and flux in high-ionization emission lines dropping well below quiescence levels (cf. the 2023-12-03 spectrum), and finally
- (4) a recovery in the accretion flow through the disk and therefore in brightness (cf. the spectrum for 2024-11-15), bringing T CrB back to or even above the photometric levels of quiescence.

4.1. Phase 1: quiescence prior to SAP

The period of quiescence of T CrB following the 1946 outburst and up to the start of SAP has been already discussed among others by Munari et al. (2016), and will not be re-investigated here. The lightcurve during this phase is dominated by the visibility of the hot spot and the ellipsoidal distortion of the red giant, which fills its Roche-lobe, inducing an orbital modulation of increasing amplitude with decreasing wavelength, reaching $\sim 0.5 \text{ mag}$ in the *V* band (see the results of radiative modeling in sect. 7 below). The faint status of the disk around the WD during quiescence allows a clean detection of the incessant flickering associated with the accretion process (cf. Sokoloski et al. 2001; Zamanov et al. 2004; Dobrotka et al. 2010, among many others). The spectrum for 2012-09-03 in the upper panel of Fig. 4 is typical of the quiescence period: at a first look it is that of a normal M3III red giant, the interacting-binary nature betrayed only by limited emission in $H\alpha$ and a weak flux excess at the shortest wavelengths

caused by the blue continuum originating from the disk and the hot spot. At a more careful evaluation, the quiescence spectra reveals the presence of other and much weaker emission lines (higher Balmer terms, HeI, HeII), but to get to them it is necessary to subtract the spectrum of a M3III template, as illustrated in Fig. 3.

It is interesting to note that the 2005-2013 quiescence part of the *B*-band lightcurve of T CrB in Fig. 1 shows a rather slow but nonetheless distinct rise in brightness, at a rate $\Delta B = -0.040 \text{ mag yr}^{-1}$, which is probably indicative of an equivalent slow rise in the accretion flow through the disk. Similarly slow and low-amplitude rising and declining trends have been a constant for T CrB in quiescence (e.g. Stanishev et al. 2004).

4.2. Phase 2: the enhanced mass-transfer phase (SAP)

As first noticed by Munari et al. (2016), T CrB left quiescence around May 2014 and begun a steady increase in brightness as a consequence of a marked and unprecedented increase in the mass flow through the disk and toward the WD, termed *enhanced mass-transfer phase* (SAP) to stress its uniqueness in the behavior that T CrB displayed since the 1946 eruption.

The maximum brightness during SAP was reached by T CrB in April-May 2016, after a smooth rise lasting two years during which the binary had time to completed 3 full orbital revolutions. In comparison with the quiescence levels in Fig. 1, at SAP peak the brightness of T CrB increased by $\Delta U = 3.4$ ($13.2 \leftrightarrow 9.8$), $\Delta B = 1.2$ ($11.5 \leftrightarrow 10.3$), $\Delta V = 0.5 \text{ mag}$ ($10.1 \leftrightarrow 9.6$), and progressively less for *R* and *I* bands; the rise in flux of HeII has been similar to that of *U*-band, amounting to $\Delta \text{HeII} = 3.0 \text{ mag}$. Soon after reaching SAP maximum, T CrB begun a slow and steady descent, at mean rates $\Delta \text{HeII} = 0.27$, $\Delta U = 0.15$, and $\Delta B = 0.05 \text{ mag yr}^{-1}$. The SAP phase sharply terminated in early May 2023 (cf. *U*-band panel at right in Fig. 1), when T CrB was still $\Delta U \sim 0.5 \text{ mag}$ brighter than average quiescence. Overall, T CrB spent two years reaching SAP maximum and seven to decline from and terminate SAP.

The spectrum of T CrB at SAP maximum is well represented by the observation for 2016-05-26 in Fig. 4. Compared to quiescence (the 2012-09-03 spectrum in the same Fig. 4), a huge increase in the continuum flux at blue wavelengths is obvious; as outstanding is the intensity of emission in the Balmer continuum. The absolute flux radiated by emission lines increased by $\sim 15\times$ compared to quiescence, with HeII 4686 turning into the third strongest line after $H\alpha$ and $H\beta$, and HeI and Bowen fluorescence at 4640 \AA being rather strong too. The difference spectrum (i.e. the SAP spectrum minus that in quiescence) closely resembles the typical spectrum of a CV in quiescence, which is dominated by the emission from the accretion disk (to this end, compare the difference spectrum in Figure 4 of Munari et al. (2016) with the mean CV spectrum of Figure 1 in Zwitter & Munari (1995) obtained at the same resolving power).

The rise to SAP maximum has been characterized by a gradual strengthening of the emission from the accretion disk (the blue and Balmer continua, the emission lines), and an increase in the ionization conditions as traced by the HeII/ $H\beta$ and HeII/HeI line ratios. The decline from SAP maximum traced back along the same evolutionary pattern followed during the rise: for ex., the spectrum for 2021-05-25 in Fig. 4, taken halfway through the *descent* from SAP maximum, is indistinguishable from the spectrum for 2015-10-16 in Figure 4 of Munari et al. (2016), obtained halfway through the *rise* to SAP maximum.

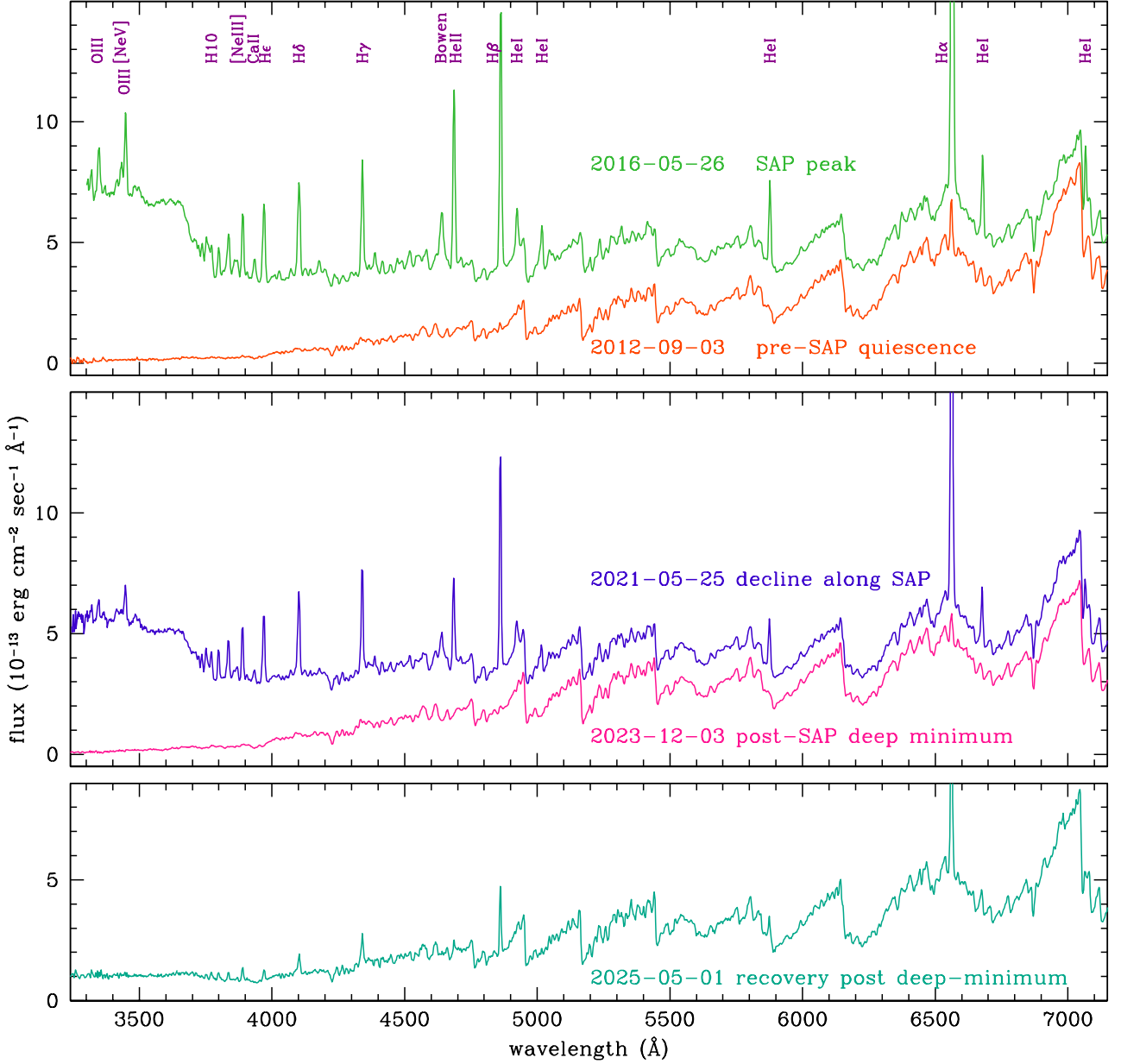


Fig. 4: Spectra of T CrB collected with the Asiago 1.22m telescope selected for being representative of the evolutionary phases T CrB has gone through during the last twenty years, as discussed in sect. 4.

The emission line profiles convey information about the amount of radiating mass and the kinematical location of the emitting regions and of those in foreground causing any superimposed absorption components. With the Asiago 1.82 + Echelle and CTIO 1.5m + Chiron telescopes we densely monitored T CrB during the SAP phase, and in Appendix B we present an atlas of the evolution of the emission line profiles for a sample of lines, namely H α , H β , HeII 4686, HeI 5876 (triplet), HeI 6678 (singlet), and [OIII] 5007. We show the profiles for selected 98 epochs (the same epochs for all lines), distributed between April 2015 and June 2023, covering the entire SAP phase. A detailed analysis and quantitative modeling of such profiles, with all their fine details and multi-components, responsive to both the accretion flow and to orbital phase, is well beyond the scopes of the present paper, and will be tackled elsewhere.

4.3. Phase 3: the post-SAP deep minimum

As well illustrated by the *U* and *M2* panels in Fig. 1, the SAP phase ended rather sharply in late April 2023, when T CrB entered a steep decline that in four months, by late August, took it close to the *U*-band brightness of the bare M3III giant, notably *well below* the median *U*-band brightness characterizing the long quiescence since the last outburst of 1946. At the time of the late August 2023 minimum, also HeII dropped below quiescence levels, while *M2* went down by 3 mag compared to SAP maximum but remained ~ 1 mag brighter than in quiescence.

After the rebound in brightness around mid-January 2024, a second drop in late March 2024 took T CrB again close to the *U*-band brightness of the bare M3III. The two minima (August 2023 and March 2024) were identical in the *BVR* bands and in the *Swift* satellite *M2* ultraviolet measurements, but they strongly differed in the behavior of HeII, which dropped almost two mag-

Table 2: Integrated HeII 4686 emission line fluxes (in units of 10^{-13} erg cm $^{-2}$ s $^{-1}$) for the flare that T CrB underwent in November 2024.

Date (UT)	HeII flux	Date (UT)	HeII flux
4.72	2.1	14.73	11.1
7.73	5.5	15.72	12.1
9.73	19.6	16.72	7.62
12.72	11.5	20.72	5.73
13.72	12.3	22.72	4.64

nitudes fainter during the second minimum compared to the first one.

The spectrum for 2023-12-03 in Fig. 4 well represents average conditions for T CrB during the protracted deep minimum phase following the end of SAP. Comparing with the typical quiescence spectrum for 2012-09-03 in the same figure, the emission in H α is clearly reduced as well as it is the veiling from the blue continuum from the disk: compare for example the depth of blue TiO bands and the visibility of CaI 4227 and CaII H&K at 3933 and 3967 Å.

4.4. Phase 4: recovery from the deep minimum

Following the passage at the second deep minimum in March 2024, T CrB has been on a rise in brightness with superimposed a lot of chaotic, short term and large-amplitude variability, which is particularly evident in the U and HeII lightcurves of Fig. 1, with photometric changes up to 1 magnitude occurring on a matter of a few days and correlating with revamp/retreat in the intensity of the blue veiling continuum and the emission lines.

The apparently brightest of such short-living episodes happened on 2024-11-16 when T CrB peaked at $B=10.72$ and $U=10.94$ as confirmed by independent observations from three different ANS Collaboration telescopes, the same three telescopes that recorded T CrB fainter by 0.6 mag in B and U both two days before and two days later. The same flare is well visible also in the intensity of HeII 4686 (and to a lesser extent in HeI and Balmer lines too), with the noteworthy feature that in HeII (and marginally in HeI too) the flare peaks a week earlier than in U and B band photometry. Our Echelle spectra obtained with the Varese 0.84m telescopes provide the integrated HeII 4686 emission line fluxes for November 2024 listed in Table 2. Combining with the HeII fluxes from low-res spectra quoted in Teyssier et al. (2024), the peak HeII flux was reached on November 9, with e-folding times of ≤ 1 day for the rise and ~ 7 days for the decline.

The rise in brightness following the second deep minimum brought T CrB well above mean quiescence and close to the level characterizing the latest stages of SAP, distinctively leveling off during the last few months before submission of this paper (see also Merc et al. 2025). The spectrum for 2025-05-01 in Fig. 4 may be considered representative of average conditions during this leveling off. Compared with the typical quiescence spectrum for 2012-09-03 in the same figure, T CrB is currently more active, with much stronger emission in Balmer, HeI, and HeII lines and a Balmer continuum clearly in emission above the reinforced blue continuum veiling the spectrum of the red giant at the shortest wavelengths. After the deep minima of August 2023 and March 2024, the mass flow through the inner radii of the accretion disk is back at the levels of the latest stages of SAP and well above that typical for the long quiescence phase following the 1946 nova eruption.

4.5. Comparing SAP in 1936-1945 and 2015-2023

Just prior to the 1946 eruption, T CrB underwent a SAP phase similar to that experienced in 2015-2023, a fact leading Munari et al. (2016) to be the first to speculate about an approaching new eruption, a view later shared by many (eg. Luna et al. 2020; Zamanov et al. 2023; Schaefer 2023b), resulting in an intensified pre-eruption monitoring of T CrB and the submission of ready-to-be-triggered proposals to most of the ground and space observing facilities.

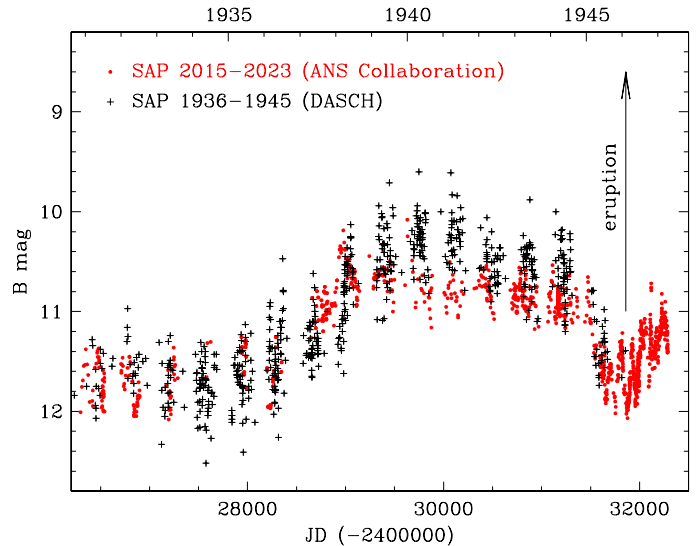


Fig. 5: Comparison between the SAP phase that T CrB underwent prior to the 1946 outburst and the 2015-2023 recent one.

The recent and the historic SAP phases (1936-1945 and 2015-2023) are compared in Fig. 5. The DASCH digitization of Harvard historical photographic plates (Grindlay et al. 2012) have been accessed to retrieve the historical data. The two SAP phases look rather similar, especially in the overall duration, as well as in the rise- and the decline-rates. As discussed below, the SAP event probably corresponds to the accretion disk flushing toward the WD most of the mass accumulated during the inter-outburst long interval. The close similarity of the 1936-1945 and 2015-2023 events suggests that the occurrence of SAP is triggered by the disk reaching an upper limit to its stable configuration after decades of steady mass transfer from the Roche-lobe filling RG companion. There are however a couple of discrepancies in the two SAP phases:

- the 1946 nova eruption happened about six months after the SAP was concluded, while the recent SAP ended more than 2 years ago and T CrB has not yet undergone a new outburst;
- the overall radiated brightness has been larger (by about 40%) for the SAP preceding the 1946 nova eruption than for the current one.

The radiated brightness relates to the amount of mass flowing through the disk, so it is tempting to deduce from the above two points that there has been yet no new outburst following the end of the 2015-2023 SAP phase because - compared to 1936-1945 - not enough mass has been so far transferred from the disk to the WD to reach ignition conditions for a thermonuclear runaway. Over the last year, T CrB has however experienced a recovery to higher-than-quiescence rates in the flow through the disk, which could make up for the deficit in the mass accumulated on the

WD surface and eventually lead to the much anticipated new eruption.

5. Radiated luminosity and mass accreted by the WD

Combining the *Swift* observations in the W2, M2 and W1 ultraviolet bands with the Asiago 1.22m + B&C spectra (or *UBVR* photometry for the epochs when Asiago spectra are not available), it is possible to reconstruct fairly well the spectral energy distribution (SED) of T CrB over the 1700-8000 Å range, as illustrated in Fig. 6, where the SED at four sample epochs is compared to that of the template M3III star HD 112300, constructed from IUE and Asiago spectra, dereddened and flux-scaled to the Gaia DR3 distance of T CrB. By subtracting the SED of the scaled M3III template to that of any epoch in which a *Swift* observation is available at least in the M2 band, we have obtained the corresponding SED associated to the accretion process. Its integration returns the accretion luminosity radiated over the 1700-8000 Å range; for illustrative purposes and for a few sample epochs, in Fig. 6 such luminosity is computed separately for the optical (3500-8000 Å) and the UV (1700-3500 Å) parts, to highlight the dominance of the latter.

The *Swift* W2 filter is known to be affected by red-leak, which comes into play when very red objects are observed. In quiescence, the disk of T CrB is faint and most of the flux recorded through the W2 filter (which nominal ultraviolet transmission starts at 1600 and peaks at 1900 Å) comes from the RG through the red leak, making the observations in this filter useless (cf. SED for 2008-2011 in Fig. 6). When however the disk brightens and the ultraviolet flux increases, as during SAP, the effect of the red-leak becomes irrelevant and the W2 measurements can be safely incorporated into building the SED (cf. SED for 2021-07-10 in Fig. 6).

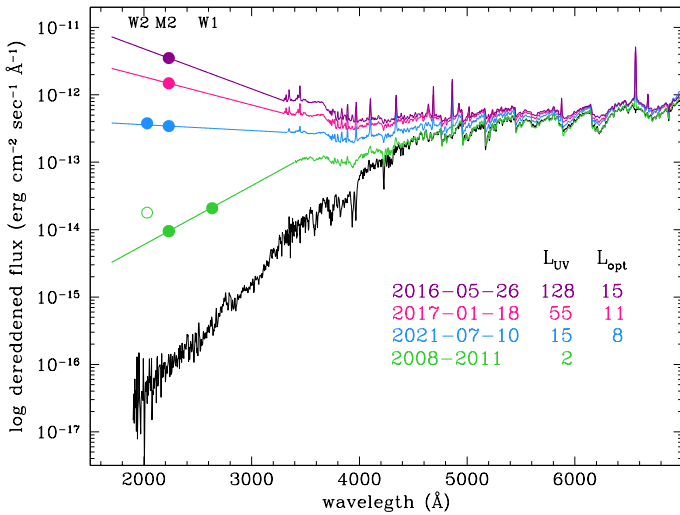


Fig. 6: Examples of the spectral energy distribution of T CrB from quiescence (2008-2011) to SAP peak (2016), and for reference that of the M3III template HD 112300, plotted in black and scaled to the distance of T CrB. Quoted L_{UV} and L_{opt} are the accretion luminosities (in L_{\odot}) radiated over the 1700-3500 and 3500-8000 Å intervals, respectively. Note on the SED for 2008-2011 the effect of the red-leak affecting the *Swift* W2 filter.

The SAP and following phases have been fairly well covered by *Swift* and near-simultaneous optical observations, so that

the evolution of the accretion luminosity can be accurately followed, with the caveat that *Swift* did not observe T CrB during the broad peak of 2016. The 2016 has been however densely covered by spectroscopic observations, and the integrated flux of the HeII 4686 line can be used to estimate the corresponding flux at M2 wavelengths. To this aim we have compared the integrated flux of the HeII 4686 line and the flux at M2 effective wavelength for the many SAP epochs in which the two values have been measured within a 2-day delay, to minimize the disturbance by the short term variability characterizing T CrB. We found a good proportionality of the two reddening-corrected values in the form:

$$\log(\text{flux}[M2]) = 0.927 \times \log(\text{flux}[HeII]) - 1.515 \quad (1)$$

In the process we found that the integrated flux of the HeII 4686 emission line also strongly correlates with the *U*-band brightness in the form corrected for reddening:

$$\log(\text{flux}[HeII]) = -0.5025 \times U - 6.229 \quad (2)$$

In both relations the flux is expressed in $\text{erg cm}^{-2} \text{s}^{-1}$. Eq.(1) then allows us to reconstruct the SED also during the broad SAP peak of 2016 by using the many measurements available for HeII.

By integrating the SEDs over 2015-2025, we found that during SAP T CrB radiated over the interval 1700-8000 Å a total accretion luminosity of:

$$L_{acc}^{SAP}[UV - opt] = 6.7 \times 10^{43} \text{ erg} \quad (3)$$

with

$$M_{acc}^{SAP}[UV - opt] = 2.6 \times 10^{-7} M_{\odot} \quad (4)$$

as the corresponding mass accreted by the WD of $1.35 M_{\odot}$; such a total splits into yearly percentages (%) of 9.4, 19.5, 18.4, 15.0, 12.4, 7.7, 6.3, 5.5, 2.5, 1.9, and 2.8 going from 2015 to 2025.

The quiescence phase following the 1946 eruption has not been mapped equally well. For sake of discussion and considering the self-similar spectroscopic appearance that T CrB maintained during the whole quiescence, we may suppose that the accretion luminosity $L_{acc} \sim 2 L_{\odot}$ derived in Fig. 6 as the mean value for 2008-2011 apply also to the rest of the quiescence; under such circumstances the total accretion luminosity radiated over the interval 1700-8000 Å during 1947-2014 then becomes:

$$L_{acc}^{quiesc}[UV - opt] = 1.6 \times 10^{43} \text{ erg} \quad (5)$$

with a corresponding accreted mass of

$$M_{acc}^{quiesc}[UV - opt] = 6.3 \times 10^{-8} M_{\odot} \quad (6)$$

The sum of $M_{acc}^{SAP}[UV - opt]$ and $M_{acc}^{quiesc}[UV - opt]$ leads to $M_{acc}[UV - opt] = 3.2(\pm 1.1) \times 10^{-7} M_{\odot}$ as the mass (so far) accreted in the inter-outburst period. This value stems from the accretion luminosity radiated longward of 1700 Å, so it has clearly to be considered as a lower limit to the true effective value (see for ex. Skopal 2015). The mass needed to trigger the outburst in conditions resembling those of T CrB ranges over $0.2-2 \times 10^{-6} M_{\odot}$ according to various theoretical models, as for example those of Yaron et al. (2005), Shen & Bildsten (2009), or Starrfield et al. (2025), much depending on the assumptions - in addition to differences in the models - on the composition and radial structure of the underlying WD, how the chemical mixing between the accreted shell and the underlying WD actually takes place, the detailed chemical and isotopic composition of the matter accreted from the companion, and so forth. What is worth noticing here is the satisfactory agreement between the accreted mass we derived above from available observations and that required in theoretical models to ignite an explosive outburst for the conditions prevailing in T CrB.

6. Orbital solution

The radial velocity (RV) of the RG has been measured via cross-correlation on the high-resolution spectra of T CrB that we collected with the Asiago 1.82m + Echelle and SMARTS 1.5m + CHIRON telescopes, with Table D.1 reporting the results of our measurements. The template for cross-correlation was selected from the synthetic spectral library of Munari et al. (2005) for the resolving power 20,000, with atmospheric parameters $T_{\text{eff}}=3500$ K, $\log g=1.5$, $[\text{Fe}/\text{H}]=0.0$, $[\alpha/\text{H}]=0.0$, $\zeta=2$ km s⁻¹. The choice of a synthetic spectrum nulls the combined effects of telluric absorptions, limited S/N, and errors in the wavelength calibration intrinsic to any RV standards observed nightly along with the target. In addition, a synthetic spectrum also nulls the effect of the jitter caused by the atmosphere of a cool giant to be deeply convective, extended, and ultimately too unstable to serve as an accurate RV standard. To check for any offset to RVs that the choice of a synthetic spectrum could introduce, we have selected from the Gaia DR3 catalog eight M2-M4 giants among those listed with the lowest uncertainty on their RV, and observed them with the Asiago 1.82m + Echelle telescope along with T CrB. Their RVs were derived via cross-correlation against the same synthetic template spectrum used for T CrB. The mean difference with the RV listed in Gaia DR3 is 0.10 ± 0.27 km s⁻¹, confirming the absence of any systematic offset.

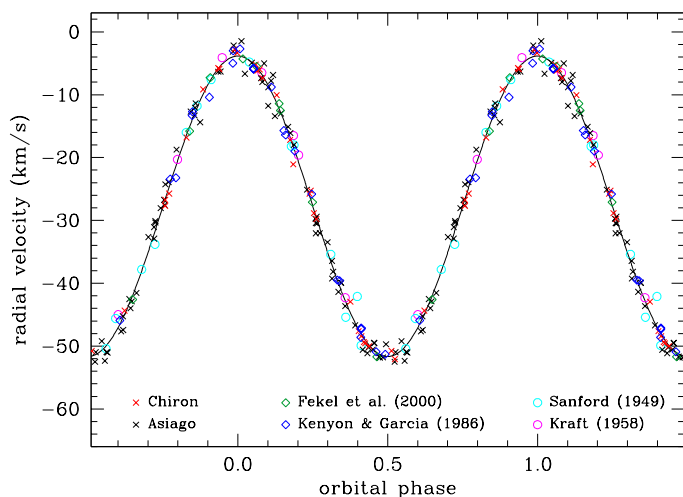


Fig. 7: The orbital solution derived in Table 3 overplotted to our Asiago and Chiron radial velocities and those of Sanford (1949), Kraft (1958), Kenyon & Garcia (1986), and Fekel et al. (2000).

Table 3: Spectroscopic orbit of the M3III in T CrB derived by combining our Asiago and Chiron radial velocities with those listed by Sanford (1949), Kraft (1958), Kenyon & Garcia (1986), and Fekel et al. (2000). T_0 is the time of passage at ascending quadrature (maximum velocity).

Parameter	Value	Error
Period (days)	227.5528	0.0002
T_0 (HJD)	2459978.37	0.08
Barycentric velocity (km s ⁻¹)	-27.75	0.04
Semi-amplitude (km s ⁻¹)	23.90	0.05
Eccentricity	0	
Mass function	0.322	0.002

A spectroscopic orbit for the cool giant in T CrB has been previously derived by Kenyon & Garcia (1986) and Fekel et al. (2000). Combining our RVs with theirs, and including the 1946-47 data of Sanford (1949) and the 1956-57 from Kraft (1958) allow us to cover a time-span of more than 28200 days (~124 orbits), well constraining the orbital parameters and the period in particular. The resulting orbital solution for the RG in T CrB is listed in Table 3 and overplotted to the data in Fig. 7. A null eccentricity is clearly supported by the data, in agreement with previous studies, and we fixed it to 0 in deriving the orbit. The rms of the data from the orbital solution is 0.89 km s⁻¹ for Chiron, 1.39 for Asiago, 1.08 for Kenyon & Garcia (1986), 1.25 for Fekel et al. (2000), 1.79 for Sanford (1949), and 1.24 for Kraft (1958).

We have performed rather extensive measurements of the emission lines present on our Echelle spectra of T CrB, recorded during SAP, hoping to be able to trace or at least constraining the motion of the WD companion. The line profiles during SAP are however highly variable and complex, and so different from line to line for the same orbital phase that no matter which way and in how many components they are deconvolved, a clean and unambiguous tracer of the WD motion could not be promptly identified. Several and different absorption and emission components superimpose along any given line of sight, apparently more responsive to the disk and hot spot brightness than to the orbital phase. This is clearly demonstrated by the atlases of line profiles during SAP, which are arranged according to the orbital phase, that we present in Appendix B for the time interval 2015-14-05 to 2023-06-01, and confirmed in Appendix C by the dense mapping in high resolution of the H α profile that we have carried out at ~1-week cadence since the end of SAP, from 2023-06-01 to 2025-05-01.

The lines grow in complexity of the emission profile and in the multiplicity of absorption components for orbital phases 0.4 to 0.8, i.e. between the passage of the RG at descending quadrature and its transit at inferior conjunction. The line-of-sight during this phase interval traverses the densest and inner strata of the RG atmosphere, crosses the hot spot and the inflated outer rim of the disk around it, aligns with the fraction of the accretion stream that may continue past the hot spot, before finally reaching the hottest inner radii of the disk: such a richness of emitting and absorbing bodies aligned along the line-of-sight, each one animated by largely different and continuously varying radial velocities, clearly calls for highly complex and lively lines profiles, and the atlases presented in Appendix B and Appendix C are a testimony to that.

The situation was apparently simpler during the long quiescence (not covered by our observations that were triggered by T CrB entering SAP), when Stanishev et al. (2004) were able to derive a good-looking sinusoidal motion from the H α emission component in anti-phase with that of the RG, clearly supporting a WD appreciably more massive than the RG.

7. Radiative modeling

The accurate *UBVRI* photometry collected by ANS Collaboration and covering both the quiescence and SAP phases allows to derive a detailed radiative model of T CrB. In this paper we will limit our analysis of the photometry to an assessment of the fraction of the Roche Lobe filled by the RG, and to quantify the role and position of the hot spot in phase-reckoned lightcurves. The position relates to the azimuth, which in turn fixes the outer radius of the disk; the latter governs the maximum orbital in-

Table 4: Binary and disk parameters depending on WD mass and orbital inclination for the mass function $f(m)=0.322$ derived from orbital solution in Table 3. Azimuths are angles in degrees counted from the line joining the two stars, positive in the direction of disk rotation. M_{WD} and M_{RG} are the mass of the WD and RG, i and a the orbital inclination and separation, R_{RG} is the radius of the Roche lobe. r_i and V_i are the closest distance to WD and the velocity at the point of the accretion stream on a fly-by trajectory around the WD (thus r_i is the minimum radius of the disk to intercept the stream, at $\sim 159^\circ$ azimuth). r_c , θ_c , and V_c are the disk's circularization radius and for the impacting stream the corresponding azimuth and velocity. r_o , θ_o , and V_o are the corresponding values for the outer disk radius in the $r_o=2\times r_c$ approximation. Finally, the last column reports about eclipsing of the hot spot by the RG ('grz' standing for grazing condition).

M_{WD} (M_\odot)	M_{RG} (M_\odot)	i ($^\circ$)	a (R_\odot)	R_{RG} (R_\odot)	Intercept		Circularization			Outer			HS eclip.
					r_i (R_\odot)	V_i (km/s)	r_c (R_\odot)	θ_c ($^\circ$)	V_c (km/s)	r_o (R_\odot)	θ_o ($^\circ$)	V_o (km/s)	
1.35	1.05	65.0	209.9	75.1	13.1	191.6	28.3	52.2	116.4	56.6	19.8	65.1	yes
1.30	0.96	65.0	205.8	72.7	13.4	184.7	28.2	52.9	114.7	56.4	19.5	64.1	yes
1.25	0.88	65.0	201.7	70.4	13.6	180.5	28.1	53.2	112.6	56.2	19.8	63.1	yes
1.35	0.93	61.5	206.4	71.1	14.1	183.4	28.9	53.4	115.4	57.9	19.6	64.7	grz
1.30	0.85	61.5	202.4	69.4	14.3	178.9	28.9	52.8	113.7	57.7	18.8	63.6	grz
1.25	0.78	61.5	198.5	67.3	14.5	173.7	28.8	54.0	112.0	57.5	19.2	62.6	grz
1.35	0.76	56.5	200.9	66.0	15.6	172.9	30.2	54.0	113.7	60.4	18.6	63.5	no
1.30	0.69	56.5	197.1	63.8	15.7	169.5	30.2	52.2	111.1	60.4	17.6	62.2	no
1.25	0.63	56.5	193.3	61.7	15.9	164.0	30.3	53.2	109.0	60.5	17.8	61.0	no

clination that still avoids eclipsing the hot spot, and ultimately affect the mass of the red giant.

We adopt the same radiative modeling carried out by Munari (2023a) in computing the synthetic lightcurve of the secondary maximum during the 1946 outburst of T CrB, and its description will be not repeated here, except adding that for the radial dependence of the temperature of the disk we followed the standard profile $T(r) = T_0(R_{\text{WD}}/r)^{3/4}(1 - \sqrt{R_{\text{WD}}/r})^{1/4}$ (cf. Warner 1995), where R_{WD} and M_{WD} are the radius and mass of the WD and $T_0 = [(3GM_{\text{WD}}\dot{M})/(8\pi\sigma R_{\text{WD}}^3)]^{1/4}$ relates to the \dot{M} mass accretion flow through the disk. The masses of the RG and WD, and the orbital inclination, have to satisfy the mass function 0.322 derived in the orbital solution of Table 3, with the orbital period and zero phase taken verbatim from it.

A sample representation of the 3D view produced by our radiative modeling is shown in Fig. 8, relative to T CrB during the quiescence phase prior to SAP, and separately for the passage of the RG at superior conjunction (phase 0.25) and descending quadrature (phase 0.5), for the parameters on the 4th line from top of Table 4, those providing the best fit to photometric lightcurves. The computed synthetic lightcurves are compared to the observed ones in Fig. 9, separately for quiescence (top panels) and SAP phases (bottom panels). Concerning the main goals stated the opening of this section, the results in Fig. 9 indicates that:

- the RG fills completely its Roche lobe; even a modest under-filling by 3% would cause a drop by 0.10 mag of the overall brightness, incompatible with Fig. 9. Maslennikova et al. (2023) concluded the same from modeling in the infrared;
- the quiescent lightcurve constrains the azimuth of the hot spot (HS) to be $20\pm 10^\circ$; the effective angular dimension of the HS as seen from the WD is about 23° , with a peak temperature of 5910 K declining to 5080 K at the HS periphery;
- the low temperature of the HS precludes it from being an important site of formation for HeII emission lines, in agreement with the results from the Doppler tomography performed by Planquart et al. (2025) that favors a formation in the inner parts of the disk;

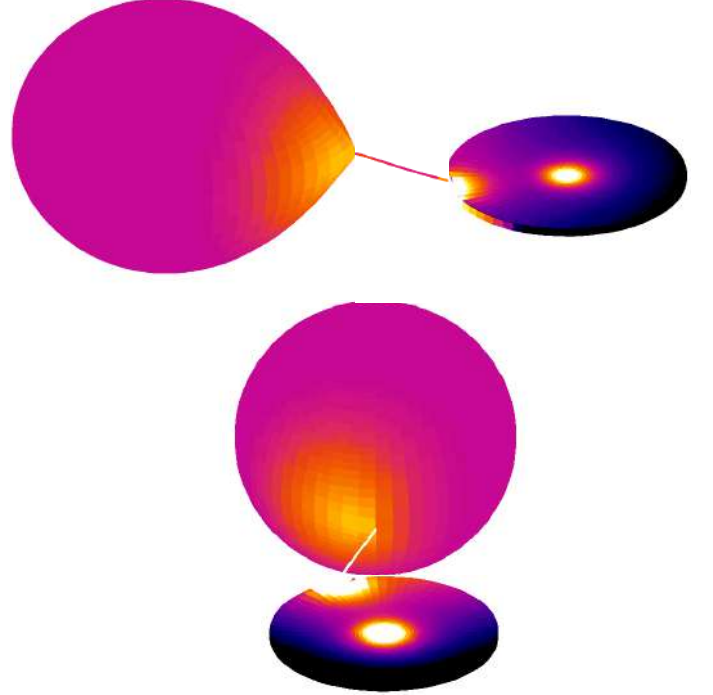


Fig. 8: 3D-views of T CrB in quiescence from the radiative modeling carried out in sect. 7, for the RG filling completely its Roche lobe, the disk extending to the standard outer radius of twice its circularization value, an orbital inclination of 61.5° , and masses of the WD and the RG of 1.35 and $0.93 M_\odot$, respectively (cf. Tab. 4). The stretching of the black-to-white color palette is different for the RG and for the disk + hot spot, respectively 3450–3600 K and 1400–1900 K.

- coupled with the dynamic trajectory of the accretion stream, the azimuth of HS implies that the outer radius r_o of the disk extends to twice the circularization radius r_c , as expected in a standard disk (Warner 1995). An outer radius equal to r_c

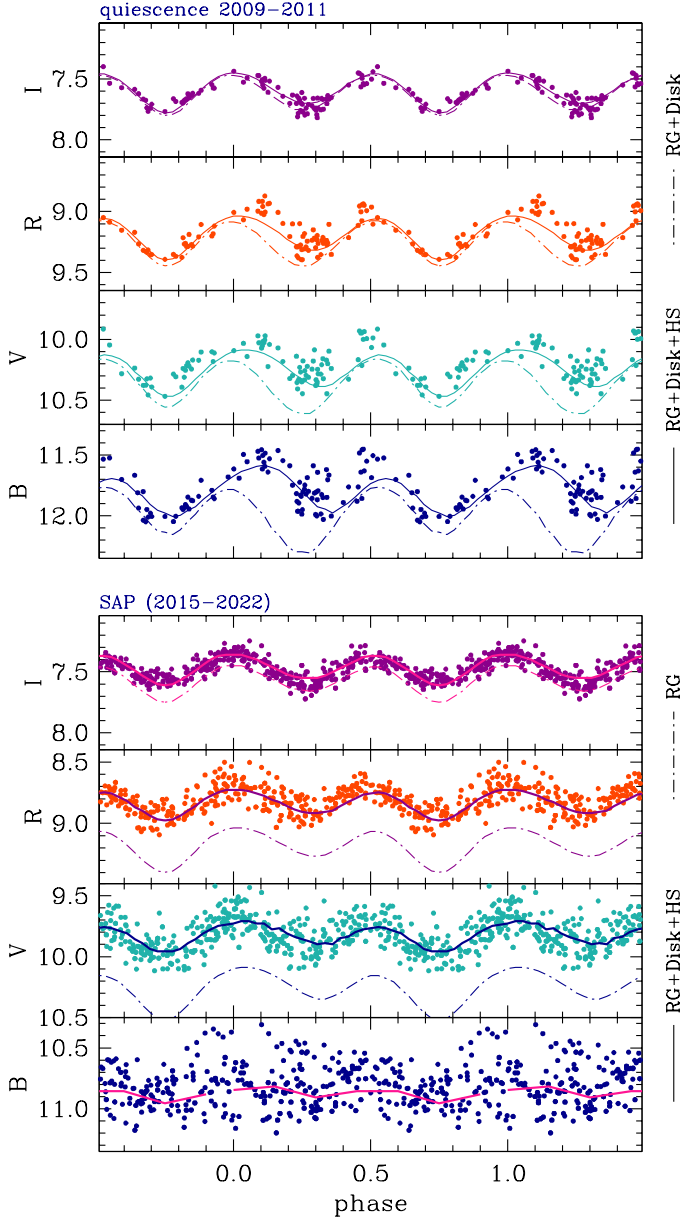


Fig. 9: The lightcurve of T CrB, separately for quiescence and SAP, is fitted with the radiative modeling described in sect. 7 and the same parameters leading up to the 3D view of Fig. 8. In the panels for quiescence at the top, the two sets of fitting curves differ by the inclusion of the hot spot (following the parameters listed in sect. 7); in the panels for SAP at the bottom, the solid curve is the fitting considering the full system, while the dot-dashed curve isolates the contribution of the sole RG.

would move the azimuth of the HS to $\sim 53^\circ$, and to $\sim 159^\circ$ if equal the minimum represented by the intercept radius r_i (cf. Table 4);

- the HS irradiates the facing side of the RG, rising the surface temperature from 3500 K to a peak value of 3560 K reached at the sub-HS point (yellowish color in Fig. 8). It also irradiates the closer portion of the disk, slightly rising the local temperature above that corresponding to the pure accretion flow (purple-to-pink color in Fig. 8);
- no matter the actual value of \dot{M} , in quiescence the outer parts of the disk remain much cooler than the surface of the RG and completely neutral: in spite of their large angular extent

(similar to that of the RG), they do not appreciably contribute to the overall brightness of T CrB at optical wavelengths;

- the HS contributes significantly to the overall brightness of T CrB in quiescence even in V and R bands. This fact strongly supports the counter-intuitive results by Munari et al. (2021) and Merc et al. (2024) for the detectability of flickering in symbiotic stars (SySts). Merc et al. (2024) was able to isolate flickering signatures from *TESS* ultra-precise observations of SySts from space, in spite of the fact that *TESS* observes in white-light over the entire optical range and therefore should be vastly dominated by the direct emission from the RG. Thanks to highly-accurate, ground-based photometry in the B band, Munari et al. (2021) have been able to detect flickering at a few milli-mag level from SySts accreting at such low levels that their nature is betrayed only by a faint emission in H α on high-resolution spectra, which becomes visible only *after* the subtraction of a template spectrum for the RG;
- the HS plays such an important role in shaping the lightcurve of T CrB that any change in its brightness or in the radius of the disk (and therefore in the azimuth of HS) would significantly alter the times of passage at minimum system brightness; HS variability developing on long time scales, as those reported by Stanishev et al. (2004), could impact attempts to detect a change in the orbital period by comparing minima in the lightcurves before and after the 1946 outburst;
- a large amplitude flickering has been observed at each of the many visits paid to T CrB during quiescence, implying that the HS is not eclipsed. The maximum orbital inclination that still avoids eclipses of the HS by the RG is 61.5° . From the 0.322 mass function and for a WD mass of $\sim 1.35 M_\odot$ (as generally adopted in theoretical models of T CrB), such an orbital inclination returns a mass of $0.93 M_\odot$ for the RG (cf. Table 4), well below the typical mass for field, single M3III giant (eg. Cox 2000). Given the Roche-lobe filling status of the RG, much of the missing mass could have been transferred to the WD, and there retained to favor its growth toward the Chandrasekhar limit. In accordance with the high retention efficiency ($[M_{\text{acc}} - M_{\text{ej}}]/M_{\text{acc}}$) recently discovered by Starrfield et al. (2025), the many nova outbursts that T CrB has underwent in its life have evidently not altered the mass-gaining path followed by the WD;
- the accretion disk, which remains faint during quiescence, dominates instead the lightcurve during SAP, contributing significantly even in the I band to the overall brightness; during SAP the relative importance of the HS on the system brightness is greatly diminished compared to quiescence. An HS similar to quiescence may still be present during SAP, as expected considering that the RG keeps spilling mass via L_1 even during SAP. The fact however that during SAP the HS does *not* turn brighter than quiescence, implies that SAP is not triggered by an increased mass-loss rate of the RG but is instead caused by some radial collapse of the disk that enhances the mass-flow toward the innermost radii and ultimately toward the WD;
- in this interpretation, the initial ~ 70 yrs of the ~ 80 yrs intra-outburst period are primarily spent in building up mass in the disk, mass that is then flushed toward the WD primarily during the last ~ 10 yrs of the intra-outburst period, giving rise to SAP-like events;
- the radial collapse of the disk seems to propagate to the outer regions at later epochs. In fact, the I-band lightcurve on the right panel of Fig. 1 maintains the SAP level well through the deep-minimum phase, until mid 2024 when it drops to

the value of the bare RG, simultaneously with the reprisal in brightness at shorter wavelengths powered by a regain in the mass flow at inner radii.

8. Rotational velocity

Zamanov et al. (2006, 2007) derived the rotational velocity of the RG in symbiotic stars from the width of absorption lines measured on FEROS spectra obtained at 48,000 resolving power. They inferred that $\sim 90\%$ of the S-type RGs have $V_{\text{rot}} \sin i$ in the interval $4.5 - 11.7 \text{ km s}^{-1}$, rotate faster than single field giants of similar spectral type, and are corotating (synchronized) with the orbital revolution. From their infrared spectra recorded at 44,000 resolving power, Fekel et al. (2004) derived for the RG of T CrB a rotational velocity $V_{\text{rot}} \sin i = 5.1 \text{ km s}^{-1}$, while Hinkle et al. (2025) obtained $V_{\text{rot}} \sin i = 8.7 \text{ km s}^{-1}$ from optical spectra at a low 15,000 resolving power.

Our Chiron spectrum for 2022-08-16 has been recorded at a much higher resolving power than either Fekel et al. (2004) and Hinkle et al. (2025), allowing us to derive a more accurate value of $V_{\text{rot}} \sin i$. For an instrumental line-spread function (LSF) with a Gaussian shape and for low rotational velocity, the observed width of stellar lines can be expressed as:

$$\sigma_{\text{obs}}^2 = (\sigma_{\text{rot}} \sin i)^2 + \sigma_{\text{LSF}}^2 + \sigma_{\xi}^2 \quad (7)$$

where σ_{ξ} is the microturbulent velocity. For the M3III giant in T CrB Wallerstein et al. (2008) derived $\sigma_{\xi} = 2 \text{ km s}^{-1}$.

Isolated telluric lines provide an efficient way to estimate σ_{LSF} because they illuminate the spectrograph slit in exactly the same way as the stellar seeing disk, providing a more accurate estimate than using lines from the comparison lamp or the sky background, which illuminates the slit uniformly. Usually σ_{LSF} degrades moving away from the center of the spectrograph's optical path because of aberrations, so to exploit the best Chiron resolving power we looked for the telluric O_2 band centered at 6278 \AA that is recorded by Chiron close to the center of central order N.48. From seven unbled lines belonging to the O_2 telluric band we derived $\sigma_{\text{LSF}} = 0.0306 \pm 0.0030$ corresponding to a local resolving power of $\lambda/\Delta\lambda = 87,200$.

The width of stellar lines σ_{obs} must obviously be measured at the same position of the telluric lines used to estimate σ_{LSF} to exploit similar optical performance by the spectrograph. From ten isolated stellar lines interspersed with the O_2 telluric ones we derive $\sigma_{\text{obs}} = 0.1124 \pm 0.0089$, from which we finally obtain: $V_{\text{rot}} \sin i = 4.75 \pm 0.26 \text{ km s}^{-1}$. For an inclination of $i = 61.5^\circ$, such velocity corresponds to corotation at a stellar radius of $24.3 R_{\odot}$. From the radiative modeling in sect. 7, the radius of the RG filling its Roche lobe is $\sim 71 R_{\odot}$ (cf. the fifth column of Table 4), for which the corotation velocity would be $V_{\text{rot}} = 16.0 \text{ km s}^{-1}$. The RG in T CrB is therefore far from corotation conditions, as if the outer layers of the RG are removed via spilling through L_1 at a rate faster than it is required to achieve corotation. In fact, the theoretical time-scale for synchronization would be just a few hundreds years following Zamanov et al. (2007), orders of magnitude shorter than the time spent by T CrB in the symbiotic mass-transfer phase.

9. Conclusions

The large body of multi-wavelength observations assembled for T CrB both during the quiescence following the 1946 outburst and in particular during the recent 2015-2023 enhanced mass-transfer phase, together with the results of orbital solution and

radiative modeling, have allowed to draw a consistent picture of T CrB and how its WD accretes the mass that is required to trigger the outburst.

The RG completely fills its Roche lobe and it is not corotating, a possible consequence of the continuous removal of its outer layers by the incessant spilling through L_1 . The material lost by the RG goes to form a disk around the WD. The $\sim 20^\circ$ azimuth of the bright hot spot formed by the impacting accretion stream fixes the outer radius of the disk to $\sim 58 R_{\odot}$, twice the circularization radius as in the standard theory of accretion disks. The hot spot is not eclipsed, and its 23° angular extension and mild temperature (5900 K degrading to 5100 K at the periphery) make it well visible in the lightcurve of T CrB even at V and R bands. For a WD of $1.35 M_{\odot}$, the orbital and radiative modeling return an inclination of 61° and a mass of $0.93 M_{\odot}$ for the RG, making the mass-transfer dynamically stable. The RG has been stripped out of the outer 0.3-0.5 solar masses, exposing to mass-transfer toward the WD the internal layers which composition (chemical and isotopic) should significantly differ from the Solar mixture generally assumed in theoretical models of the outburst.

The hot spot did not brighten during the enhanced mass-transfer phase, indicating that SAP is not triggered by an increase in the mass loss from the RG but is instead caused by the inside-out collapse of the accretion disk grown in mass beyond the stable configuration. The disk seems spending the initial ~ 70 of the ~ 80 yrs intra-outburst period mainly to grown in mass, transferring to the WD only a limited amount of what it is gaining; it is during the last ~ 10 of the ~ 80 yrs intra-outburst interval that most of the mass-transfer to the WD takes place, in a 4:1 proportion and at mean rate ~ 28 faster than in quiescence.

Comparing with the enhanced mass-transfer phase that preceded the 1946 outburst, the present one attained a lower brightness, suggesting that a lower amount of mass has been transferred from the disk to the WD. This could justify the delay affecting the outburst, not yet occurred two full years past the end of the enhanced mass-transfer phase while in 1946 it followed just 6 months after.

While the inner parts of the disk emptied during the enhanced mass-transfer phase which ended in late April 2023, the outer parts started migrating inward, and from \sim May 2024 begun restoring the mass-flow at shorter radii with the noticeable effect that the brightness of T CrB in the optical and ultraviolet rose back to levels higher than in quiescence. The consequent revamp in the accretion rate toward the WD could fill any deficit left over by the under-luminous 2015-2023 enhanced mass-transfer phase, and ultimately lead the shell accumulated on the surface of the WD to reach ignition conditions. The material restoring the mass-flow at the inner radii of the disk migrated inward from the outer parts of the disk which radiates primarily in the far red/IR: in fact, simultaneous with the re-brightening in the blue and UV that started in May 2024, T CrB became fainter in the I band almost down to the brightness of the bare red giant.

10. Data availability

Tables 1 and A.1 are only available in electronic form at the CDS via anonymous ftp to cdsarc.u-strasbg.fr (130.79.128.5) or via <http://cdsweb.u-strasbg.fr/cgi-bin/qcat?J/A+A/>. The spectroscopic data presented in this paper are also available via CDS.

Acknowledgements. We acknowledge the anonymous Referee for useful and constructive comments. This work has been in part supported by INAF 2023 MiniGrant Program (contract C93C23008470001 to UM). NM acknowledges financial support through ASI-INAF and 'Mainstream' agreement 2017-14-H.0

(PI: T. Belloni). This work has made use of data provided by Digital Access to a Sky Century @ Harvard (DASCH), which has been partially supported by NSF grants AST-0407380, AST-0909073, and AST-1313370. Work on DASCH Data Release 7 received support from the Smithsonian American Women's History Initiative Pool. Part of this work is based on archival data, software or online services provided by the Space Science Data Center - ASI.

References

- Anupama, G. C. & Prabhu, T. P. 1991, *MNRAS*, 253, 605
- Bessell, M. S., Castelli, F., & Plez, B. 1998, *A&A*, 333, 231
- Blackburn, J. K. 1995, in *Astronomical Society of the Pacific Conference Series*, Vol. 77, *Astronomical Data Analysis Software and Systems IV*, ed. R. A. Shaw, H. E. Payne, & J. J. E. Hayes, 367
- Breeveld, A. A., Landsman, W., Holland, S. T., et al. 2011, in *American Institute of Physics Conference Series*, Vol. 1358, *Gamma Ray Bursts 2010*, ed. J. E. McEnery, J. L. Racusin, & N. Gehrels (AIP), 373–376
- Cassatella, A., Patriarichi, P., Selvelli, P. L., et al. 1982, in *ESA Special Publication*, Vol. 176, *Third European IUE Conference*, ed. E. Rolfe & A. Heck, 229–231
- Cox, A. N. 2000, *Allen's astrophysical quantities* (Springer)
- Dobrotka, A., Hric, L., Casares, J., et al. 2010, *MNRAS*, 402, 2567
- Fekel, F. C., Hinkle, K. H., & Joyce, R. R. 2004, in *IAU Symposium*, Vol. 215, *Stellar Rotation*, ed. A. Maeder & P. Etenens, 168
- Fekel, F. C., Joyce, R. R., Hinkle, K. H., & Skrutskie, M. F. 2000, *AJ*, 119, 1375
- Gaia Collaboration. 2016, *A&A*, 595, A1
- Gaia Collaboration. 2023, *A&A*, 674, A1
- Gehrels, N., Chincarini, G., Giommi, P., et al. 2004, *ApJ*, 611, 1005
- Grindlay, J., Tang, S., Los, E., & Servillat, M. 2012, in *IAU Symposium*, Vol. 285, *New Horizons in Time Domain Astronomy*, ed. E. Griffin, R. Hanisch, & R. Seaman, 29–34
- Henden, A. & Munari, U. 2006, *A&A*, 458, 339
- Henden, A. & Munari, U. 2008, *Baltic Astronomy*, 17, 293
- Hinkle, K. H., Nagarajan, P., Fekel, F. C., et al. 2025, *arXiv e-prints*, [arXiv:2502.20664](https://arxiv.org/abs/2502.20664)
- Hric, L., Petrik, K., Urban, Z., Niarchos, P., & Anupama, G. C. 1998, *A&A*, 339, 449
- Iijima, T. 1990, *Journal of AAVSO*, 19, 28
- Kenyon, S. J. 1986, *The symbiotic stars* (Cambridge Univ. Press)
- Kenyon, S. J. & Garcia, M. R. 1986, *AJ*, 91, 125
- Kraft, R. P. 1958, *ApJ*, 127, 625
- Kukarkin, B. V. 1946, *IAU Circ.*, 1038, 1
- Landolt, A. U. 1992, *AJ*, 104, 340
- Landolt, A. U. 2009, *AJ*, 137, 4186
- Luna, G. J. M., Sokoloski, J. L., Mukai, K., & M. Kuin, N. P. 2020, *ApJ*, 902, L14
- Maslennikova, N. A., Tatarnikov, A. M., Tatarnikova, A. A., et al. 2023, *Astronomy Letters*, 49, 501
- Merc, J., Beck, P. G., Mathur, S., & García, R. A. 2024, *A&A*, 683, A84
- Merc, J., Wyrzykowski, Ł., Beck, P. G., et al. 2025, *arXiv e-prints*, [arXiv:2504.20592](https://arxiv.org/abs/2504.20592)
- Munari, U. 2023a, *Research Notes of the American Astronomical Society*, 7, 251
- Munari, U. 2023b, *Research Notes of the American Astronomical Society*, 7, 145
- Munari, U. 2025, *Contributions of the Astronomical Observatory Skalnaté Pleso*, 55, 47
- Munari, U., Bacci, S., Baldinelli, L., et al. 2012, *Baltic Astronomy*, 21, 13
- Munari, U., Dallaporta, S., & Cherini, G. 2016, *New A*, 47, 7
- Munari, U. & Moretti, S. 2012, *Baltic Astronomy*, 21, 22
- Munari, U., Sordo, R., Castelli, F., & Zwitter, T. 2005, *A&A*, 442, 1127
- Munari, U., Traven, G., Masetti, N., et al. 2021, *MNRAS*, 505, 6121
- Munari, U., Yudin, B. F., Taranova, O. G., et al. 1992, *A&AS*, 93, 383
- Munari, U. & Zwitter, T. 1997, *A&A*, 318, 269
- Nikolov, Y. 2022, *New A*, 97, 101859
- Page, M. J., Kuin, N. P. M., Breeveld, A. A., et al. 2013, *MNRAS*, 436, 1684
- Payne-Gaposchkin, C. & Wright, F. W. 1946, *ApJ*, 104, 75
- Planquart, L., Jorissen, A., & Van Winckel, H. 2025, *A&A*, 694, A85
- Poole, T. S., Breeveld, A. A., Page, M. J., et al. 2008, *MNRAS*, 383, 627
- Raikova, D. & Antov, A. 1986, *Information Bulletin on Variable Stars*, 2960, 1
- Roming, P. W. A., Kennedy, T. E., Mason, K. O., et al. 2005, *Space Sci. Rev.*, 120, 95
- Sanford, R. F. 1949, *ApJ*, 109, 81
- Schaefer, B. E. 2023a, *MNRAS*, 524, 3146
- Schaefer, B. E. 2023b, *Journal for the History of Astronomy*, 54, 436
- Schlafly, E. F. & Finkbeiner, D. P. 2011, *ApJ*, 737, 103
- Shears, J. H. 2024, *Research Notes of the American Astronomical Society*, 8, 233
- Shen, K. J. & Bildsten, L. 2009, *ApJ*, 692, 324
- Skopal, A. 2015, *New A*, 36, 116
- Sokoloski, J. L., Bildsten, L., & Ho, W. C. G. 2001, *MNRAS*, 326, 553
- Stanishev, V., Zamanov, R., Tomov, N., & Marziani, P. 2004, *A&A*, 415, 609
- Starrfield, S., Bose, M., Woodward, C. E., et al. 2025, *ApJ*, 982, 89
- Teyssier, F., Sims, F., Guarro, J., Bertand, E., & Shore, S. N. 2024, *The Astronomer's Telegram*, 16912, 1
- Tokovinin, A., Fischer, D. A., Bonati, M., et al. 2013, *PASP*, 125, 1336
- Wallerstein, G., Harrison, T., Munari, U., & Vanture, A. 2008, *PASP*, 120, 492
- Warner, B. 1995, *Cataclysmic variable stars*, Vol. 28 (Cambridge Univ. Press)
- Yaron, O., Prialnik, D., Shara, M. M., & Kovetz, A. 2005, *ApJ*, 623, 398
- Zamanov, R., Bode, M. F., Stanishev, V., & Martí, J. 2004, *MNRAS*, 350, 1477
- Zamanov, R., Boeva, S., Latev, G. Y., et al. 2023, *A&A*, 680, L18
- Zamanov, R. K., Bode, M. F., Melo, C. H. F., et al. 2007, *MNRAS*, 380, 1053
- Zamanov, R. K., Bode, M. F., Melo, C. H. F., et al. 2006, *MNRAS*, 365, 1215
- Zamanov, R. K. & Zamanova, V. I. 1997, *Information Bulletin on Variable Stars*, 4461, 1
- Zwitter, T. & Munari, U. 1995, *A&AS*, 114, 575

Appendix A: Swift UVOT observations of T CrB

In order to trace the evolution of T CrB in the near-UV, we selected a series of pointings performed over nearly two decades, between 2008 and 2025, with the UltraViolet Optical Telescope (UVOT; Roming et al. 2005) onboard the Neil Gehrels *Swift* satellite (Gehrels et al. 2004), which observed in the *UVW1* (2600 Å), *UVM2* (2246 Å), and *UVW2* (1928 Å) filters. See sect. 2.3 for details about the measurements of these data.

Table A.1: Archive Swift UVOT observations of T CrB.

Obs. ID	Date	UT start	expt (sec)	W2	M2	W1	W2	M2	W1
				(Vega system magnitudes)			(fluxes $\times 10^{-15} \text{cm}^{-2} \text{s}^{-1} \text{\AA}^{-1}$)		
00035171006	2008-03-16	20:32:24	269	14.44±0.04			9.0±0.3		
00035171006	2008-03-16	20:41:41	255			13.67±0.04			13.6±0.5
00035171006	2008-03-16	20:37:03	269		14.64±0.04			6.5±0.2	
00035171006	2008-03-17	02:56:24	269	14.38±0.04			9.5±0.3		
00035171006	2008-03-17	03:01:02	269		14.82±0.05			5.47±0.18	
00035171006	2008-03-17	03:03:41	255			13.87±0.04			11.3±0.4
00045776001	2011-11-27	12:09:33	542	14.17±0.04			11.5±0.4		
00045776001	2011-11-27	12:18:49	542		14.84±0.04			5.36±0.15	
00045776001	2011-11-27	12:28:06	465			13.69±0.04			13.4±0.5
00045776001	2011-11-28	02:50:12	364		14.96±0.04			4.82±0.15	
00045776001	2011-11-28	02:43:57	364	14.55±0.04			8.1±0.3		
00045776001	2011-11-28	02:56:27	385			13.79±0.04			12.1±0.5
00045776002	2011-12-04	09:38:49	363			13.56±0.04			15.1±0.6
00045776002	2011-12-04	09:24:23	421	14.10±0.04			12.3±0.4		
00045776002	2011-12-04	09:31:36	421		14.60±0.04			6.72±0.19	
00081659002	2015-09-24	02:37:18	1632	10.13±0.10			470±50		
00045776004	2015-10-01	01:01:23	151	9.92±0.12			570±70		
00045776005	2017-01-18	04:15:03	1174		9.26±0.10			920±90	
00045776005	2017-01-18	05:49:17	1219		9.30±0.10			880±90	
00045776005	2017-01-18	07:25:17	1219		9.28±0.10			900±90	
00045776005	2017-01-18	10:41:22	919		9.34±0.10			860±90	
00045776005	2017-01-18	11:58:48	1366		9.30±0.10			880±90	
00045776005	2017-01-18	13:34:15	1457		9.24±0.10			930±90	
00045776005	2017-01-18	15:17:25	916		9.30±0.10			880±90	
00045776005	2017-01-18	17:00:24	975		9.35±0.10			850±90	
00045776005	2017-01-18	20:21:06	580		9.40±0.11			810±90	
00045776007	2017-02-08	13:41:45	247		9.39±0.11			820±90	
00045776007	2017-02-08	21:58:15	217		9.41±0.11			800±90	
00045776026	2017-09-26	02:03:43	662		9.63±0.11			650±70	
00045776026	2017-09-26	10:01:44	1605		9.53±0.10			710±70	
00045776026	2017-09-26	16:41:57	708		9.55±0.10			700±70	
00045776026	2017-09-26	21:24:02	585		9.57±0.11			690±80	
00045776026	2017-09-26	23:15:14	395		9.48±0.11			740±80	
00045776027	2017-10-27	10:44:33	730		9.26±0.10			920±90	
00045776032	2018-07-27	03:37:45	541		10.60±0.04			266±6	
00011548001	2019-09-04	02:34:46	127		10.18±0.13			400±50	
00011548001	2019-09-04	08:55:36	138		9.62±0.12			660±80	
00011548001	2019-09-04	15:28:21	93		10.05±0.13			440±60	
00013922001	2020-12-06	00:51:42	191		10.71±0.04			241±6	
00012011005	2021-07-10	08:47:26	147		10.89±0.04			205±5	
00012011006	2021-07-10	09:02:03	51	10.99±0.04			214±8		
00012011013	2021-08-24	02:28:32	200		10.76±0.04			231±5	
00013558010	2022-03-08	14:05:24	149		10.60±0.04			266±6	
00013558017	2022-06-22	07:49:39	193		10.67±0.04			249±6	
00013558035	2022-12-10	19:22:45	124			11.14±0.04			140±5
00013558035	2022-12-10	19:27:11	249	11.09±0.04			196±6		
00013558035	2022-12-10	19:32:35	197		11.23±0.04			149±3	
00013558041	2023-01-10	17:56:20	153		10.74±0.04			235±6	
00013558053	2023-03-10	16:20:13	160		10.66±0.04			253±6	
00013558067	2023-05-12	19:00:09	154	11.20±0.04			178±6		
00013558067	2023-05-12	19:03:33	82		11.27±0.04			144±4	
00013558072	2023-05-25	23:11:29	126			11.31±0.04			119±5
00013558072	2023-05-25	23:15:59	252	11.30±0.04			161±4		

Table A.1: continued.

Obs. ID	Date	UT start	expt (sec)	W2	M2	W1	W2	M2	W1
				(Vega system magnitudes)			(fluxes $\times 10^{-15} \text{cm}^{-2} \text{s}^{-1} \text{\AA}^{-1}$)		
00013558072	2023-05-25	23:21:28	145		11.49 \pm 0.04			118 \pm 3	
00013558078	2023-06-09	10:37:24	130			11.78 \pm 0.04			78 \pm 3
00013558078	2023-06-09	10:42:02	261	11.64 \pm 0.04			118 \pm 4		
00013558078	2023-06-09	10:47:41	191		11.85 \pm 0.04			85 \pm 2	
00013558093	2023-07-09	17:21:09	223		12.66 \pm 0.04			40.0 \pm 1.0	
00013558092	2023-07-09	23:29:46	127			12.17 \pm 0.04			54 \pm 2
00013558092	2023-07-09	23:34:17	215	12.37 \pm 0.04			60.1 \pm 1.8		
00013558107	2023-08-08	10:56:08	119			12.88 \pm 0.04			28.0 \pm 1.1
00013558107	2023-08-08	11:00:23	238	13.45 \pm 0.04			22.4 \pm 0.7		
00013558107	2023-08-08	11:05:33	140		13.47 \pm 0.04			18.9 \pm 0.6	
00013558121	2023-09-05	01:50:33	79			12.97 \pm 0.04			25.8 \pm 1.1
00013558121	2023-09-05	01:53:27	157	13.48 \pm 0.04			21.6 \pm 0.8		
00013558121	2023-09-05	01:56:56	117		13.78 \pm 0.05			14.3 \pm 0.5	
00013558139	2023-10-03	18:01:39	85			13.13 \pm 0.04			22.2 \pm 0.9
00013558139	2023-10-03	18:04:46	171	13.39 \pm 0.04			23.6 \pm 0.8		
00013558139	2023-10-03	18:08:32	142		13.43 \pm 0.04			19.8 \pm 0.5	
00013558155	2023-10-28	18:17:34	139			13.22 \pm 0.04			20.5 \pm 0.8
00013558155	2023-10-28	18:20:07	137	13.19 \pm 0.04			28.4 \pm 0.8		
00013558155	2023-10-28	18:23:10	104		13.48 \pm 0.05			18.8 \pm 0.6	
00013558161	2023-11-28	14:27:15	130			13.04 \pm 0.04			24.2 \pm 0.9
00013558161	2023-11-28	14:31:52	260	13.39 \pm 0.04			23.7 \pm 0.6		
00013558161	2023-11-28	14:37:32	200		13.56 \pm 0.04			17.4 \pm 0.5	
00013558167	2023-12-12	21:58:16	133			12.82 \pm 0.04			29.7 \pm 1.1
00013558167	2023-12-12	22:02:59	265	13.31 \pm 0.04			25.3 \pm 0.8		
00013558167	2023-12-12	22:08:43	189		12.71 \pm 0.04			38.1 \pm 0.9	
00013558173	2023-12-26	19:40:53	104			12.44 \pm 0.04			42.3 \pm 1.6
00013558173	2023-12-26	19:44:40	208	13.02 \pm 0.04			33.1 \pm 1.1		
00013558173	2023-12-26	19:49:14	159		13.09 \pm 0.04			27.0 \pm 0.7	
00013558185	2024-01-23	01:31:24	129			11.96 \pm 0.04			66 \pm 3
00013558185	2024-01-23	01:35:58	257	12.48 \pm 0.04			54.4 \pm 1.7		
00013558185	2024-01-23	01:41:33	199		12.59 \pm 0.04			42.6 \pm 1.0	
00013558193	2024-02-06	18:32:37	78			12.72 \pm 0.04			32.5 \pm 1.3
00013558193	2024-02-06	18:38:52	121		13.01 \pm 0.04			29.1 \pm 0.8	
00013558193	2024-02-06	18:35:27	155	12.81 \pm 0.04			40.3 \pm 1.3		
00097564005	2024-04-11	17:14:59	173			13.33 \pm 0.04			18.5 \pm 0.7
00097564006	2024-04-11	17:33:32	82	13.87 \pm 0.05			15.2 \pm 0.6		
00097564004	2024-04-11	20:24:59	882		13.79 \pm 0.04			14.2 \pm 0.3	
00097564020	2024-05-11	11:37:11	177			11.59 \pm 0.04			92 \pm 3
00097564020	2024-05-11	11:32:36	266		11.84 \pm 0.04			85 \pm 2	
00097564020	2024-05-11	11:41:53	298	11.93 \pm 0.04			90 \pm 3		
00097564039	2024-06-10	19:10:07	276		13.34 \pm 0.04			21.3 \pm 0.5	
00097564039	2024-06-10	19:14:53	184			12.89 \pm 0.04			27.8 \pm 1.1
00097564039	2024-06-10	19:19:45	306	13.37 \pm 0.04			24.1 \pm 0.7		
00097564057	2024-07-10	10:58:33	258		11.95 \pm 0.04			77.0 \pm 1.9	
00097564057	2024-07-10	11:03:00	171			11.73 \pm 0.04			81 \pm 3
00097564057	2024-07-10	11:07:32	318	11.64 \pm 0.04			118 \pm 4		
00097564075	2024-08-09	19:27:38	273		11.46 \pm 0.04			121 \pm 3	
00097564075	2024-08-09	19:32:21	182			11.17 \pm 0.04			136 \pm 5
00097564075	2024-08-09	19:37:09	341	11.52 \pm 0.04			132 \pm 4		
00097564094	2024-09-08	06:51:45	69	11.19 \pm 0.04			179 \pm 6		
00097564096	2024-09-08	10:26:44	276		11.03 \pm 0.04			179 \pm 4	
00097564120	2024-10-08	01:23:36	329		11.48 \pm 0.04			119 \pm 3	
00097564120	2024-10-08	01:29:16	219			11.30 \pm 0.04			120 \pm 5
00097564120	2024-10-08	01:35:02	407	11.35 \pm 0.04			154 \pm 4		
00097564137	2024-11-29	23:17:03	297		12.15 \pm 0.04			64.0 \pm 1.6	
00097564137	2024-11-29	23:22:10	198			11.97 \pm 0.04			65 \pm 2
00097564137	2024-11-29	23:27:23	327	12.06 \pm 0.04			80 \pm 2		
00097564143	2024-12-09	07:32:48	259		12.00 \pm 0.04			73.6 \pm 1.8	
00097564143	2024-12-09	07:37:16	172			11.80 \pm 0.04			76 \pm 3
00097564143	2024-12-09	07:41:50	183	12.10 \pm 0.04			78 \pm 2		

Table A.1: continued.

Obs. ID	Date	UT start	expt (sec)	W2	M2	W1	W2	M2	W1
				(Vega system magnitudes)			(fluxes $\times 10^{-15} \text{cm}^{-2} \text{s}^{-1} \text{\AA}^{-1}$)		
00097564161	2025-01-08	04:17:02	315		11.30 \pm 0.04			140 \pm 3	
00097564161	2025-01-08	04:22:27	209			11.09 \pm 0.04			146 \pm 6
00097564161	2025-01-08	04:27:58	411	11.22 \pm 0.04			174 \pm 6		
00097564168	2025-01-18	08:54:10	259		11.22 \pm 0.04			151 \pm 3	
00097564168	2025-01-18	08:58:38	172			11.15 \pm 0.04			139 \pm 5
00097564168	2025-01-18	09:03:12	338	11.08 \pm 0.04			197 \pm 6		
00097564174	2025-01-28	02:12:25	259		11.33 \pm 0.04			137 \pm 3	
00097564174	2025-01-28	02:16:53	172			11.15 \pm 0.04			139 \pm 5
00097564174	2025-01-28	02:21:27	323	11.18 \pm 0.04			181 \pm 6		
00097564180	2025-02-07	20:59:42	274		10.52 \pm 0.04			287 \pm 7	
00097564186	2025-02-17	15:51:59	276		10.72 \pm 0.04			240 \pm 5	
00097564192	2025-02-27	18:03:28	248		10.52 \pm 0.04			287 \pm 7	
00097564198	2025-03-09	03:36:25	275		10.92 \pm 0.04			199 \pm 4	
00097564204	2025-03-19	16:39:18	262		11.27 \pm 0.04			145 \pm 3	
00097564204	2025-03-19	16:43:49	174			11.08 \pm 0.04			148 \pm 6
00097564204	2025-03-19	16:48:26	325	11.11 \pm 0.04			192 \pm 6		
00097564210	2025-03-29	20:42:06	277		11.16 \pm 0.04			159 \pm 4	
00098285001	2025-04-03	14:43:09	749	11.03 \pm 0.04			207 \pm 6		
00098285001	2025-04-03	14:48:38	437		11.18 \pm 0.04			156 \pm 3	
00098285004	2025-04-18	13:45:36	448			11.02 \pm 0.04			156 \pm 6
00098285004	2025-04-18	13:55:06	897	11.03 \pm 0.04			207 \pm 6		
00098285004	2025-04-18	14:06:51	684		11.23 \pm 0.04			150 \pm 3	
00098285007	2025-05-03	20:27:19	444			11.34 \pm 0.04			116 \pm 4
00098285007	2025-05-03	20:36:37	890	11.57 \pm 0.04			126 \pm 4		
00098285007	2025-05-03	20:48:04	544		11.47 \pm 0.04			120 \pm 3	

Appendix B: Atlas of high-resolution emission line profiles of T CrB during SAP

In this appendix we present an atlas of high-resolution profiles of selected emission lines ($H\alpha$, $H\beta$, HeII 4686, HeI 5876, HeI 6678, and [OIII] 5007), obtained with the Asiago 1.82m + Echelle and CTIO 1.55m + Chiron telescopes, covering the SAP phase of T CrB from April 2015 to June 2023. All spectra have been continuum normalized and are plotted on the same ordinate scale for an easier comparison. The orbital phase quoted for each spectrum has been computed according to the orbital solution given in Table 3, where phase 0.0 corresponds to the passage of the RG at the ascending quadrature (maximum RG velocity).

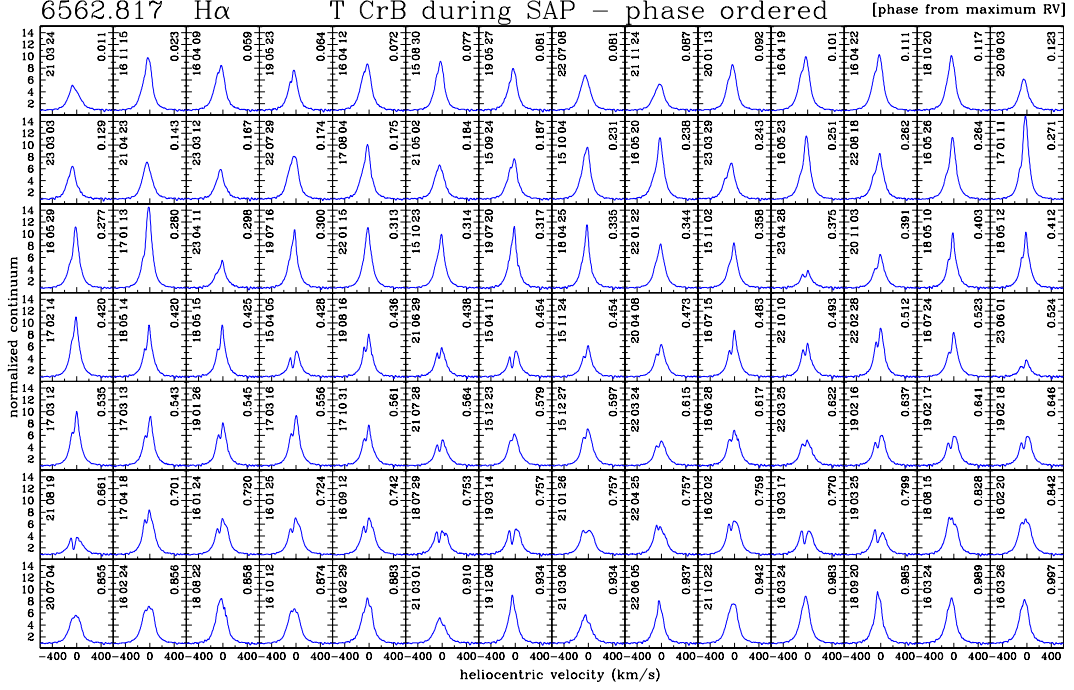


Fig. B.1: High-resolution $H\alpha$ emission line profiles of T CrB during SAP from Asiago 1.82m + Echelle and SMARTS 1.55 + Chiron observations.

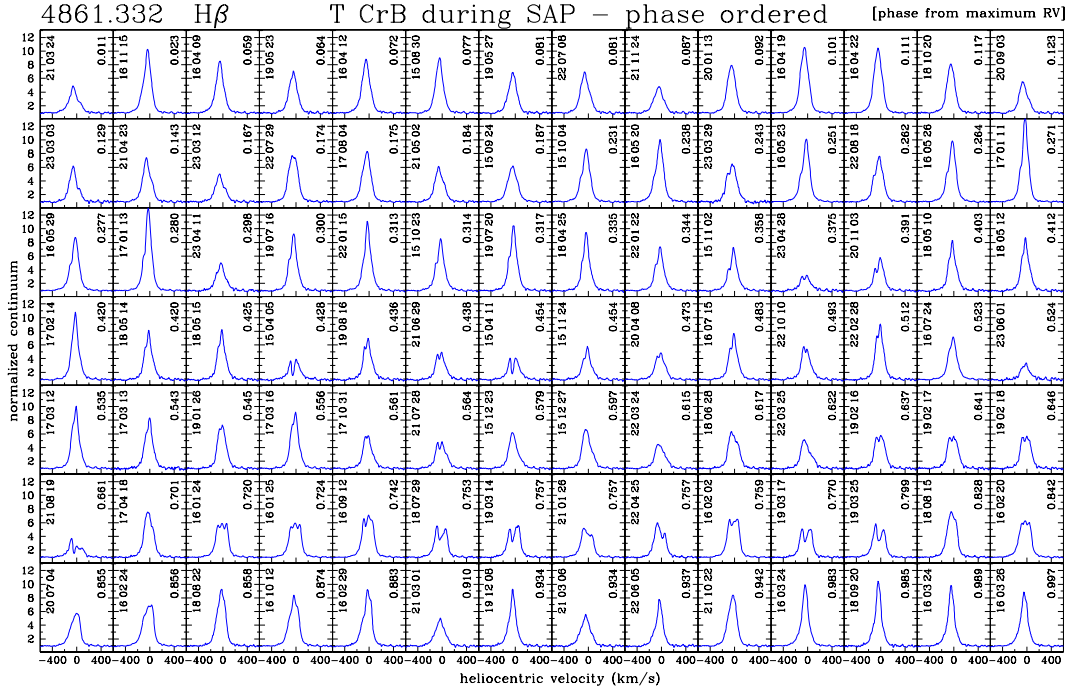


Fig. B.2: High-resolution $H\beta$ emission line profiles of T CrB during SAP from Asiago 1.82m + Echelle and SMARTS 1.55 + Chiron observations.

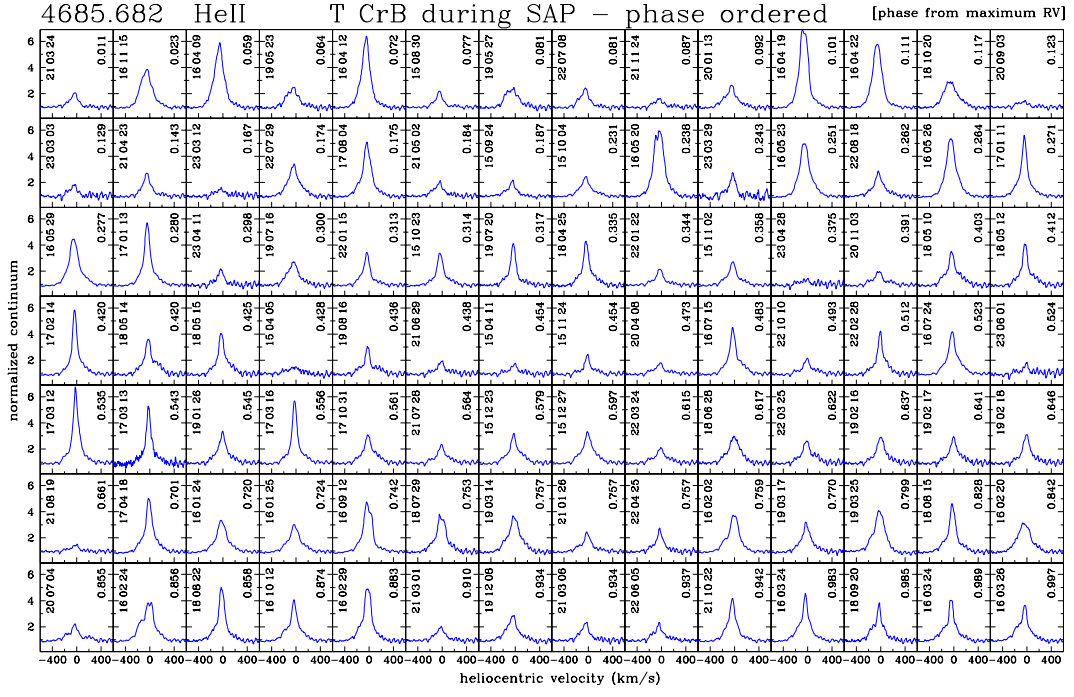


Fig. B.3: High-resolution HeII 4686Å emission line profiles of T CrB during SAP from Asiago 1.82m + Echelle and SMARTS 1.55 + Chiron observations.

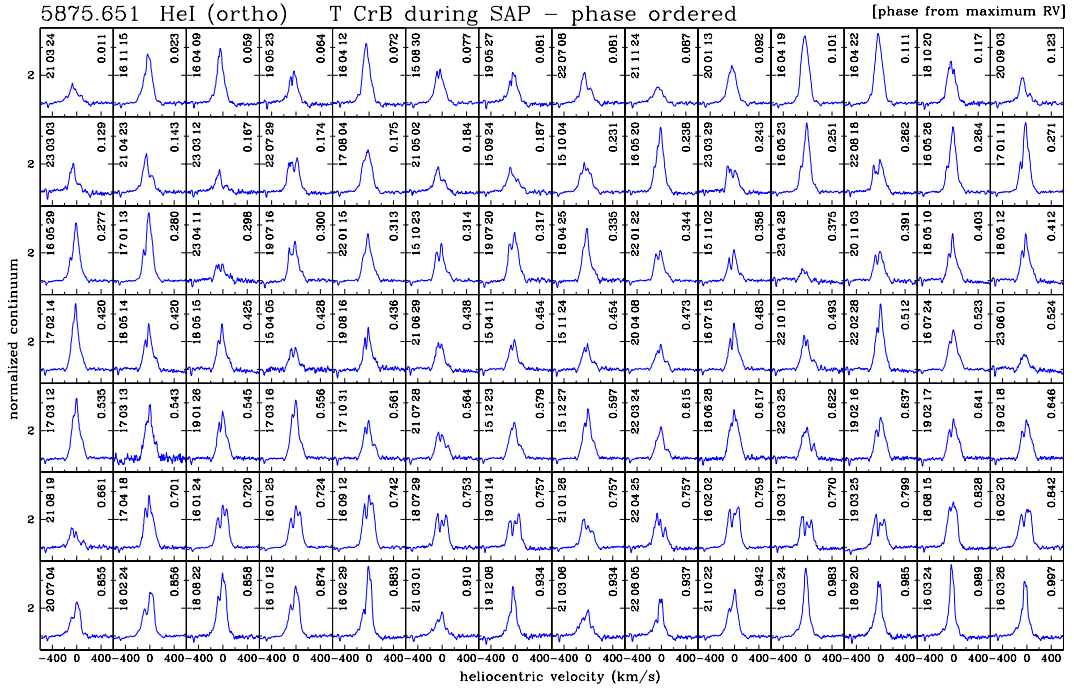


Fig. B.4: High-resolution HeI 5876Å emission line profiles of T CrB during SAP from Asiago 1.82m + Echelle and SMARTS 1.55 + Chiron observations.

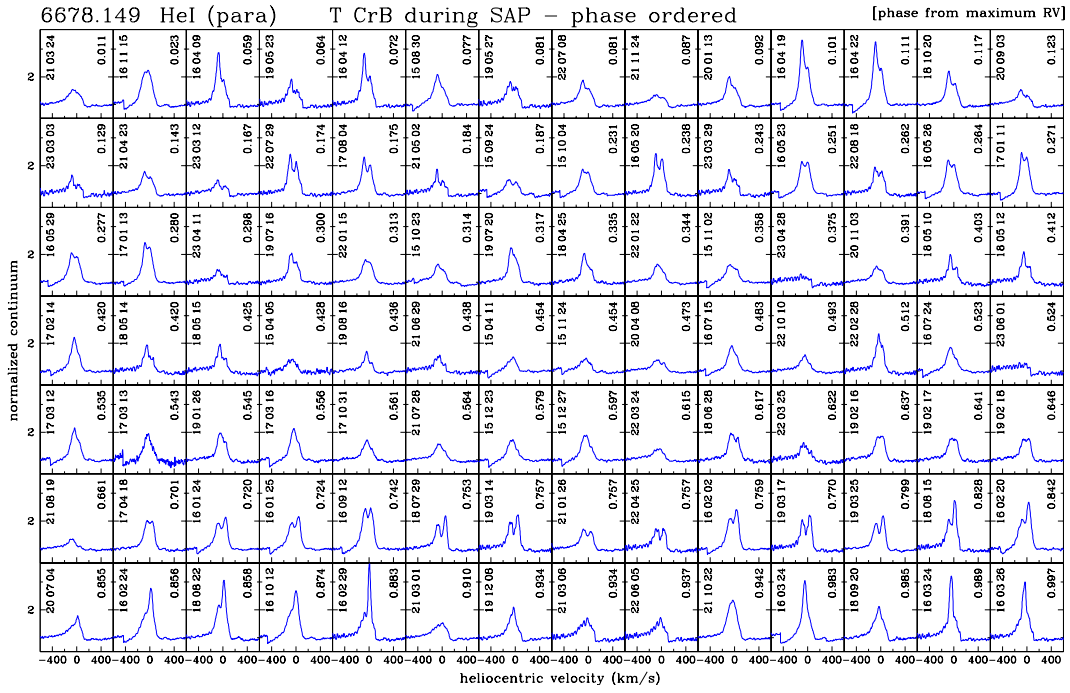


Fig. B.5: High-resolution HeI 6768Å emission line profiles of T CrB during SAP from Asiago 1.82m + Echelle and SMARTS 1.55 + Chiron observations. The occasional dent on the blue side of the line is caused by imperfect conjunction of adjacent Echelle orders.

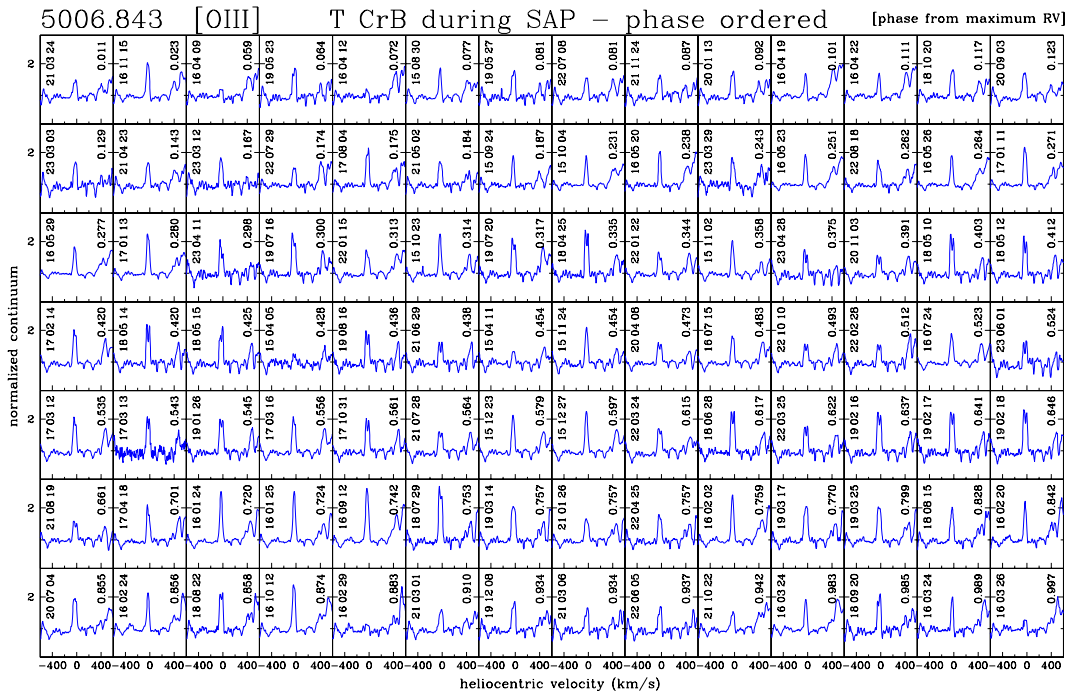


Fig. B.6: High-resolution [OIII] 5007Å emission line profiles of T CrB during SAP from Asiago 1.82m + Echelle and SMARTS 1.55 + Chiron observations.

Appendix C: Atlas of high-resolution profiles for $H\alpha$ of T CrB during post-SAP and recovery phases

In this appendix we present a selection of high-resolution profiles for the $H\alpha$ emission line of T CrB, obtained with the Varese 0.84m telescope + Multi-Mode Echelle spectrograph at a resolving power of 12,000. These profiles cover the post-SAP evolution of $H\alpha$ to present time, and thus extend the time coverage of Fig. B.1 that focuses on the SAP phase alone.

To derive clean profiles, for all the observations presented in this picture we have subtracted from the original spectra the spectrum of a template M3III giant obtained with the same telescope, shifted to the epoch velocity of the red giant in T CrB. The template spectrum is shown for reference at the bottom of the panels. Such a subtraction is particularly important to reconstruct the true profile at the time of the weakest emission in $H\alpha$, during the deep-minimum phase discussed in sect. 4.3.

The spectra, distributed over three orbits, are aligned on the three panels at the same orbital phase for ease of comparison (phase 0.0 corresponding to passage of the red giant at ascending quadrature, as per Table 3).

The upper right box illustrates (at a more dense time mapping) the rapid spectral $H\alpha$ evolution during the November 2024 flare (cf. sect. 4.4). The same flare is well visible also in the evolution of all other emission lines and particularly in HeII 4686. For sake of completeness, the bottom left box shows some spectra recorded with Asiago and CTIO telescopes in the first six months of the post-SAP period, before the monitoring with the Varese 0.84m telescope could begin.

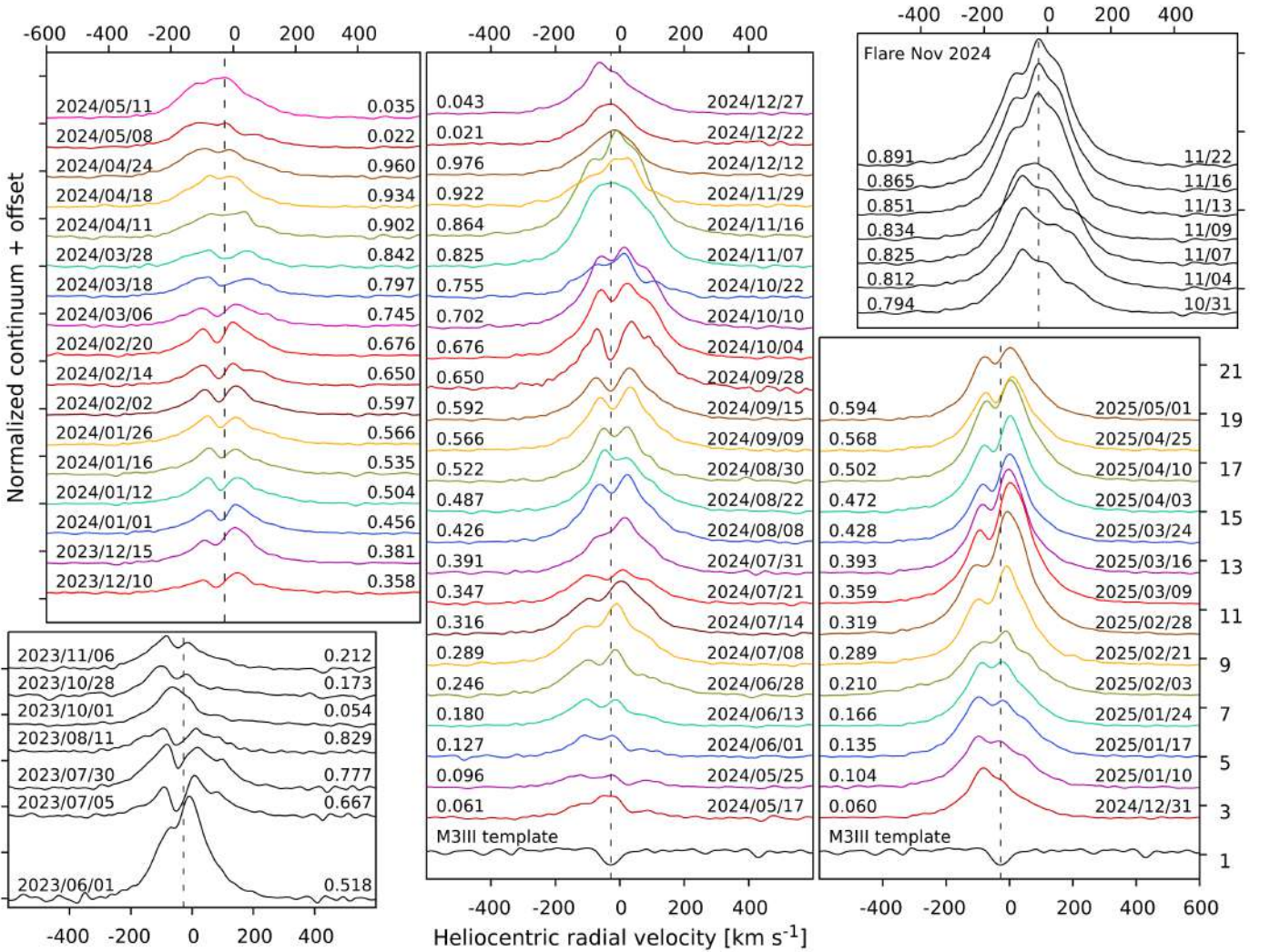


Fig. C.1: Evolution of the profile of $H\alpha$ emission line during the post-SAP phase of T CrB, from Echelle observations collected with the Varese 0.84m telescope. The dashed vertical line marks the barycentric velocity of the system.

Appendix D: Radial velocity measurements of the cool giant in T CrB

We report here the heliocentric radial velocity (RV) of the RG that has been measured via cross-correlation on the high-resolution spectra of T CrB that we collected with the Asiago 1.82m + Echelle and SMARTS 1.5m + CHIRON telescopes. The template for cross-correlation was selected from the synthetic spectral library of Munari et al. (2005) for the resolving power 20,000, with atmospheric parameters $T_{\text{eff}}=3500$ K, $\log g=1.5$, $[\text{Fe}/\text{H}]=0.0$, $[\alpha/\text{H}]=0.0$, $\zeta=2$ km s⁻¹.

Table D.1: Radial velocities of the cool giant in T CrB

Asiago 1.82m+ Echelle				SMARTS 1.5m + CHIRON	
HJD (-2400000)	RV (km/s)	HJD (-2400000)	RV (km/s)	HJD (-2400000)	RV (km/s)
55665.411	-4.92	57862.396	-32.65	57448.887	-9.16
55989.662	-51.67	57970.333	-16.09	57472.912	-2.76
56057.361	-23.91	58058.241	-50.96	57474.815	-3.36
57118.610	-51.13	58234.355	-41.36	57488.760	-5.19
57122.523	-50.56	58298.389	-47.43	57491.781	-5.97
57265.305	-7.40	58329.370	-26.73	57529.660	-25.76
57290.347	-17.96	58353.362	-11.36	58249.709	-47.62
57300.283	-25.11	58382.267	-2.15	58251.719	-48.43
57319.240	-39.25	58412.235	-6.87	58253.708	-49.36
57329.222	-43.63	58509.684	-49.20	58254.705	-49.57
57351.190	-49.53	58530.583	-42.51	58346.491	-16.81
57351.195	-49.49	58531.549	-43.97	58557.842	-27.69
57386.700	-47.65	58532.572	-42.88	58560.883	-25.72
57411.655	-31.07	58566.517	-18.74	58627.725	-6.20
57411.726	-32.90	58685.433	-38.15	58631.683	-7.34
57412.685	-30.10	58712.319	-50.22	59280.882	-5.77
57412.701	-30.34	58825.729	-6.34	59337.742	-21.07
57419.642	-27.54	58863.723	-8.81	59395.570	-50.00
57439.487	-12.68	58948.465	-51.85	59639.904	-50.76
57442.679	-12.07	59035.360	-13.31	59664.882	-44.35
57471.615	-3.12	59096.289	-13.40	59695.756	-26.73
57498.394	-11.76	59157.245	-46.70	59736.659	-5.91
57500.539	-7.77	59240.683	-24.26	59790.486	-17.19
57534.469	-30.41	59298.456	-1.48	59808.489	-28.84
57534.505	-32.05	59328.367	-12.99	59810.486	-29.79
57535.352	-30.49	59424.326	-51.02	60007.896	-10.06
57537.477	-32.03	59446.310	-41.53	60033.800	-25.26
57585.365	-51.80	59510.231	-6.32	60063.771	-42.93
57594.355	-52.49	59543.188	-5.02	60097.671	-52.08
57644.278	-28.06	59594.737	-36.43		
57674.236	-14.38	59601.700	-39.93		
57708.202	-6.67	59601.709	-39.94		
57761.729	-29.73	59663.474	-45.25		
57762.709	-29.42	59769.354	-7.97		
57797.607	-50.57	59863.267	-49.71		
57822.580	-50.98	60016.468	-15.10		
57829.428	-52.34	60046.411	-33.48		